

J-PLUS: Spectroscopic validation of $H\alpha$ emission line maps in spatially resolved galaxies

Rahna, P. T.¹, Akhlaghi, M.¹, López-Sanjuan, C.¹, Logroño-García, R.¹, Muniesa, D. J.¹, Domínguez-Sánchez, H.¹, Fernández-Ontiveros, J. A.¹, Sobral, David^{2,3}, Lumbreras-Calle, A.¹, Chies-Santos, A. L.⁴, Rodríguez-Martín, J. E.⁵, Eskandarlou, S.¹, Ederoclite, A.¹, Alvarez-Candal, A.⁵, H. Vázquez Ramió¹, A. J. Cenarro¹, A. Marín-Franch¹, J. Alcaniz⁶, R. E. Angulo^{7,8}, D. Cristóbal-Hornillos¹, R. A. Dupke^{6,9,10}, C. Hernández-Monteagudo^{11,12}, M. Moles¹, L. Sodr e Jr.¹³, and J. Varela¹

¹ Centro de Estudios de Física del Cosmos de Aragón (CEFCA), Plaza San Juan 1, 44001 Teruel, Spain
e-mail: rahna.payyasseri@gmail.com

² Departamento de Física, Faculdade de Ciências, Universidade de Lisboa, Edifício C8, Campo Grande, PT1749-016 Lisbon, Portugal

³ BNP Paribas Corporate & Institutional Banking, Torre Ocidente Rua Galileu Galilei, 1500-392 Lisbon, Portugal

⁴ Instituto de Física, Universidade Federal do Rio Grande do Sul (UFRGS), Av. Bento Gonçalves, 9500 Porto Alegre, RS, Brazil

⁵ Instituto de Astrofísica de Andalucía, CSIC, Apt 3004, E18080 Granada, Spain

⁶ Observatório Nacional - MCTI (ON), Rua Gal. José Cristino 77, São Cristóvão, 20921-400 Rio de Janeiro, Brazil

⁷ Donostia International Physics Centre (DIPC), Paseo Manuel de Lardizabal 4, 20018 Donostia-San Sebastián, Spain

⁸ IKERBASQUE, Basque Foundation for Science, 48013, Bilbao, Spain

⁹ University of Michigan, Department of Astronomy, 1085 South University Ave., Ann Arbor, MI 48109, USA

¹⁰ University of Alabama, Department of Physics and Astronomy, Gallalee Hall, Tuscaloosa, AL 35401, USA

¹¹ Instituto de Astrofísica de Canarias, La Laguna, 38205, Tenerife, Spain

¹² Departamento de Astrofísica, Universidad de La Laguna, 38206, Tenerife, Spain

¹³ Instituto de Astronomia, Geofísica e Ciências Atmosféricas, Universidade de São Paulo, 05508-090 São Paulo, Brazil

February 11, 2025

ABSTRACT

Aims. We present a dedicated automated pipeline to construct spatially resolved emission $H\alpha$ + $[NII]$ maps and to derive the spectral energy distributions (SEDs) in 12 optical filters (five broad and seven narrow/medium) of $H\alpha$ emission line regions in nearby galaxies ($z < 0.0165$) observed by the Javalambre Photometric Local Universe Survey (J-PLUS).

Methods. We used the J0660 filter of 140 Å width centered at 6600 Å to trace $H\alpha$ + $[NII]$ emission and r and i broad bands were used to estimate the stellar continuum. We create pure emission line images after the continuum subtraction, where the $H\alpha$ emission line regions were detected. This method was also applied to Integral Field Unit (IFU) spectroscopic data from PHANGS-MUSE, CALIFA and MaNGA surveys by building synthetic narrow-bands based on J-PLUS filters. The studied sample includes the cross-matched catalog of these IFU surveys with J-PLUS third data release (DR3), amounting to 2 PHANGS-MUSE, 78 CALIFA, and 78 MaNGA galaxies at $z < 0.0165$, respectively.

Results. We compared the $H\alpha$ + $[NII]$ radial profiles from J-PLUS and the IFU surveys, finding good agreement within the expected uncertainties. We also compared the SEDs from the emission line regions detected in J-PLUS images, reproducing the main spectral features present in the spectroscopic data. Finally, we compared the emission fluxes from the J-PLUS and IFU surveys accounting for scale differences, finding a difference of only 2% with a dispersion of 7% in the measurements.

Conclusions. The J-PLUS data provides reliable spatially resolved $H\alpha$ + $[NII]$ emission maps for nearby galaxies. We provide the J-PLUS DR3 catalog for the 158 galaxies with IFU data, including emission maps, SEDs of star-forming clumps, and radial profiles.

Key words. galaxy formation – emission lines – optical

1. Introduction

Spatially resolved studies of galaxies have significantly advanced our understanding of galaxy formation and evolution. Unlike previous techniques that gather integrated flux from entire galaxies, spatially resolved studies reveal local variations in different regions of galaxies, allowing the detailed understanding of different characteristics such as stellar population properties, star formation, gas kinematics, and the chemical composition in galaxies. In particular, spatially resolving galaxies has provided

new opportunities for detailed emission line studies in galaxies. For example, $H\alpha$ (6563 Å) is a prominent emission line in the optical, used as an important star formation tracer (< 10 Myr, Kennicutt 1998), which is produced from hydrogen recombination in nebular regions ionized by the radiation field of young, short-lived massive stars, and also due to the contribution from (AGN). Spatially resolved $H\alpha$ emission line maps (hereafter "emap") are crucial for understanding the star formation activity, gas dynamics, and feedback processes in galaxies.

Narrow-band (NB) imaging and integral field spectroscopy (IFS) are two key techniques that have allowed spatially resolved

* rahna.payyasseri@gmail.com

emission line studies of galaxies. The NB technique dedicated for $H\alpha$ imaging surveys (e.g., James et al. 2004; Sobral et al. 2013; Stroe & Sobral 2015; Sobral et al. 2015) has greatly improved our understanding of spatially resolved information on star formation in galaxies. However, these post NB surveys were usually limited to a few square degrees or a selected number of galaxies (e.g., 100 to 1000).

The introduction of IFS in astronomy has been a game changer for spatially resolved studies of galaxies, enabling astronomers to simultaneously gather spectra from different regions of a galaxy in the form of 3D data cubes. The TIGER instrument (Bacon et al. 1988) developed at the Observatoire de Lyon, France mounted on the Canada-France-Hawaii Telescope (CFHT) was the first instrument that demonstrated the power of IFS in astronomy. Then, more advanced optical Integral Field Unit (IFUs) like SAURON (Miller et al. 2000), VIMOS (Le Fèvre et al. 2003), SAMI (Croom et al. 2012), MUSE (Bacon et al. 2014), MaNGA (Bundy et al. 2015), and PPaK/CALIFA (Sánchez et al. 2012) were introduced into the field and these have significantly improving our understanding of galaxies, nebula, star-forming regions by offering a resolved perspective that allows for detailed analysis of their internal structures and physical processes. The earlier IFS systems such as SAURON or Tiger were lenslet-based, MaNGA and PPaK/CALIFA are fiber-based IFS, while MUSE is image slicer-based. Recently, IFUs have expanded to space-based missions such as the Near-Infrared Spectrograph (NIRSpec; Jakobsen et al. 2022) on the James Webb Space Telescope (JWST), enabling unprecedented high-resolution spectroscopy of distant galaxies. These IFSs have studied $H\alpha$ emission line maps of thousands of galaxies that allow for statistical studies of galaxy evolution, environmental effects, and the relationship between star formation and galaxy morphology (Novais & Sodré 2019; Barrera-Ballesteros et al. 2023). However, these IFUs are time-expensive and limited due to the small field of view (FoV) and limited number of observed targets.

Multiband photometric surveys such as ALHAMBRA (Advanced Large, Homogeneous Area Medium-Band Redshift Astronomical Survey; Moles et al. 2008) covering 4 deg², PAU (Physics of the Accelerating Universe; Benítez et al. 2009) covering 100 deg² have given a significant contribution to wide-field surveys and bridge the gap between broad-band photometry and IFS with their multiple filters. Javalambre Photometric Local Universe Survey (J-PLUS; Cenarro et al. 2014, 2019) and Javalambre-Physics of the Accelerating universe astrophysical Survey (J-PAS; Benitez et al. 2014; Dupke et al. 2016) are the two ongoing optical surveys in the northern sky at the Observatorio Astrofísico de Javalambre (OAJ). The large FoV, high spatial resolution and contiguous narrow-band filters covering a wide wavelength range (3300-11000 Å) of J-PAS act like a low-resolution IFU ($R \sim 60$), which is suitable for IFU-like science such as spatially resolved studies of galaxies planned over 8500 deg² (by the end of 2030). J-PLUS includes some of the narrow bands from J-PAS covering prominent emission lines such as [OII] λ 3725, $H\alpha$ + [NII] λ 6548, 6583 at $z < 0.0165$ and also [OIII] λ 5007 at $0.006 < z < 0.0473$ (Lumbreras-Calle et al. 2022) allowing us to study the spatially resolved properties of galaxies in these spectral lines. In comparison to the field of view of other time-expensive IFUs such as MaNGA (12''- 32''), SAMI (15''), PPaK/CALIFA (60''), and MUSE (60''), the uniqueness of J-PLUS is their large FoV (1.4°) offering a large contiguous observing area to understand the resolved structure of galaxies, galaxy groups, galaxy clusters and thus, probe their environment.

Table 1: Filter characteristics of J-PLUS

Name	λ_{cent} (Å)	λ_{pivot} (Å)	FWHM (Å)	Spec.line	$m_{lim}^{(a)}$ (mag)
uJAVA	3485	3523	508	–	20.8
J0378	3785	3786	168	[OII]	20.8
J0395	3950	3951	100	CaH+K	20.8
J0410	4100	4101	200	H δ	21
J0430	4300	4300	200	–	21
gSDSS	4803	4745	1409	–	21.8
J0515	5150	5150	200	[OIII]	21
rSDSS	6254	6230	1388	–	21.8
J0660	6600	6600	138	$H\alpha$ + [NII]	21
iSDSS	7668	7677	1535	–	21.3
J0861	8610	8603	400	Ca Triplet	20.4
zSDSS	9114	8922	1409	–	20.5

Note: ^(a) J-PLUS DR3 typical 5σ depths on 3'' aperture (López-Sanjuan et al. 2024)

The method of measuring $H\alpha$ fluxes and SFRs from J-PLUS photometry was first introduced by Vilella-Rojo et al. (2015) and Logroño-García et al. (2019). Vilella-Rojo et al. (2021) applied their method to estimate the star formation main sequence in the local Universe using J-PLUS DR1. Here, we aim to extend that work to validate the $H\alpha$ flux extraction for spatially resolved studies using J-PLUS DR3. We selected galaxies with redshifts up to $z \leq 0.0165$, ensuring that the J0660 NB filter covers the $H\alpha$ emission line within this range. This leads to thousands of galaxies at $D < 70$ Mpc within the 3192 deg² observed area of J-PLUS DR3. At this redshift range, J-PLUS will be able to resolve star-forming regions on the physical scale of several hundred parsecs (~ 168 pc). We validate our method of building the emaps by comparing them with other well-known IFU observations of the same galaxies. This is the first of a series of works where we aim to use the $H\alpha$ map to study the spatially resolved star formation main sequence of J-PLUS galaxies and UV and $H\alpha$ studies of J-PLUS galaxies.

This paper is organized as follows. In Sect. 2 we detail the J-PLUS, PHANGS-MUSE, CALIFA, and MaNGA data. Sect. 3 describes the sample selection. Our methods and the pipeline developed are described in Sect. 4, and the results are discussed in Sect. 5. Our final conclusions are given in Sect. 6.

2. Data

In this section, we discuss various data sets used for this study. We chose three different IFU surveys (CALIFA, MaNGA and PHANGS-MUSE) for the comparison of our method with J-PLUS. CALIFA and MaNGA were selected for their large number of local galaxies and PHANGS-MUSE was selected for its higher resolution and depth. More details about these datasets are given below.

2.1. J-PLUS DR3

J-PLUS (Cenarro et al. 2014, 2019) is a multi-band photometric survey designed to observe the northern sky in several thousand square degrees using the 80cm Javalambre Auxiliary Survey Telescope (JAST80) at OAJ, Teruel. It has 12 broad, intermediate, and narrow band optical filters with 2 deg² FoV. The properties of J-PLUS filters are given in Table 1. After two data releases (DR1 on July 2018, and DR2 on July 2020), J-PLUS had its third data release in July 2022, containing 1642 J-PLUS fields

Table 2: Comparison of the instrument properties of different IFU surveys with J-PLUS.

Parameters	J-PLUS	eCALIFA	MaNGA	PHANGS-MUSE
Telescope (m)	0.8	3.5	2.5	8
Wavelength (\AA)	3000 - 10000	3700 - 7500	3600 - 10000	4750 - 9350
Spatial Sampling ($''/\text{pixel}$)	0.55	0.5	0.5	0.2
Spectral Sampling ($\text{\AA}/\text{slice}$)	–	2	1	1.25
PSF ($''$)	1.1	1	2.54	0.7 - 1
FoV Area (arcsec^2)	25,401,600 ($1.4^\circ \times 1.4^\circ$)	3552 ($74'' \times 64''$)	93.5 ($12''$) to 665.8 ($32''$)	3600 ($59.9'' \times 60.0''$)
Spectral Resolution (\AA)	60 (for H α)	850	2000	1770 – 3590

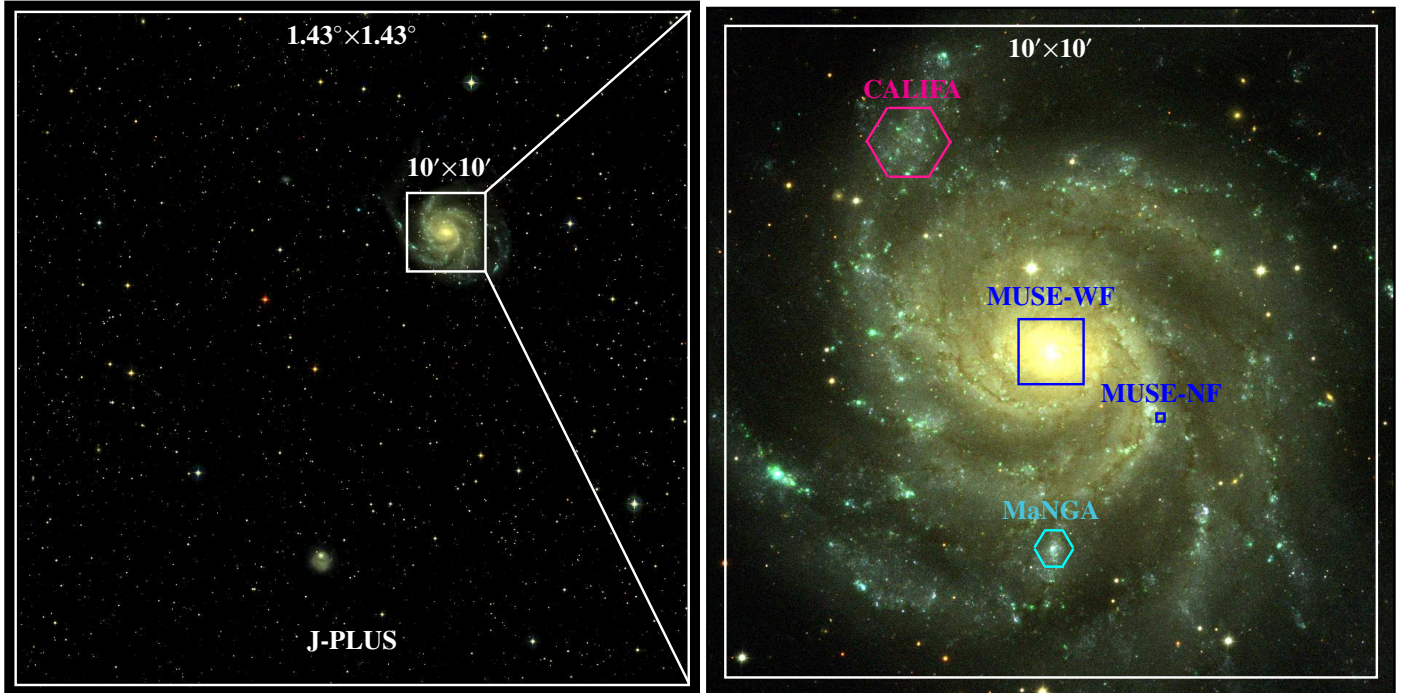


Fig. 1: Comparison of J-PLUS FoV for a single pointing with other IFUs. Left panel: The full FoV of J-PLUS (pointing 02433 including M101). Right panel: $10' \times 10'$ field of J-PLUS observation of M101 and the FoVs of MUSE in its wide-field mode ($59.9'' \times 60''$), and narrow-field mode ($7.42'' \times 7.43''$), CALIFA ($78''$) and MaNGA ($32''$) are marked.

covering 3192 deg^2 . The pixel scale of J-PLUS is $0.555''/\text{pixel}$. The point spread function (PSF) of J-PLUS observation is ~ 1.1 arcsecs in the r band. The DR3 images that we have used here are available from the OAJ database¹. The calibration and zero-points are taken from López-Sanjuan et al. (2019, 2024).

2.2. PHANGS-MUSE

The Multi-Unit Spectroscopic Explorer (MUSE; Bacon et al. 2010) is an IFS at the Very Large Telescope (VLT) of the European Southern Observatory (ESO) Paranal Observatory, Chile. It is composed of 24 identical integral-field units (IFUs). In its wide field mode (WFM; FoV of $1' \times 1'$) 90000 spectra are taken with a spatial resolution of $0.2''/\text{pixel}$ covering a wavelength range of 4750 - 9350 \AA with a spectral resolution of 2.5 \AA . The spectral resolution of MUSE is 2.5 \AA (FWHM) at 7000 \AA and the spectral sampling of 1.25 $\text{\AA}/\text{slice}$.

The PHANGS (Physics at High Angular resolution in Nearby GalaxieS) is the survey designed to observe nearby galaxies with high spatial resolution utilizing various telescopes,

such as ALMA (Leroy et al. 2021), Hubble (Lee et al. 2022), VLT/MUSE, and JWST (Lee et al. 2023) for the multiscale, multiphase study of star-formation and the interstellar medium. The PHANGS-MUSE survey (Kreckel et al. 2021) is a program with MUSE to map 19 nearby ($D \leq 20$ Mpc), massive star-forming galaxies. It provides their central star-forming disk by combining 5 to 15 MUSE pointings. This was the first IFS view of nearby star formation in different local environments. The PHANGS-MUSE observations were carried out in WFM mode. The PSF of the PHANGS-MUSE observations is between $0.7''$ and $1''$. The PHANGS-MUSE pipeline-processed data cubes are downloaded from the ESO archive². The MUSE data are not corrected for foreground Galactic extinction.

2.3. CALIFA

The Calar Alto Legacy Integral Field Area Survey (CALIFA; Sánchez et al. 2012) is a large project to obtain spatially resolved spectra of ~ 600 nearby galaxies with a size of $64''$ (diameter) in the redshift range of $0.005 < z < 0.03$ using a

¹ <https://archive.cefca.es/catalogues/jplus-dr3>

² https://archive.eso.org/scienceportal/home?data_collection=PHANGS

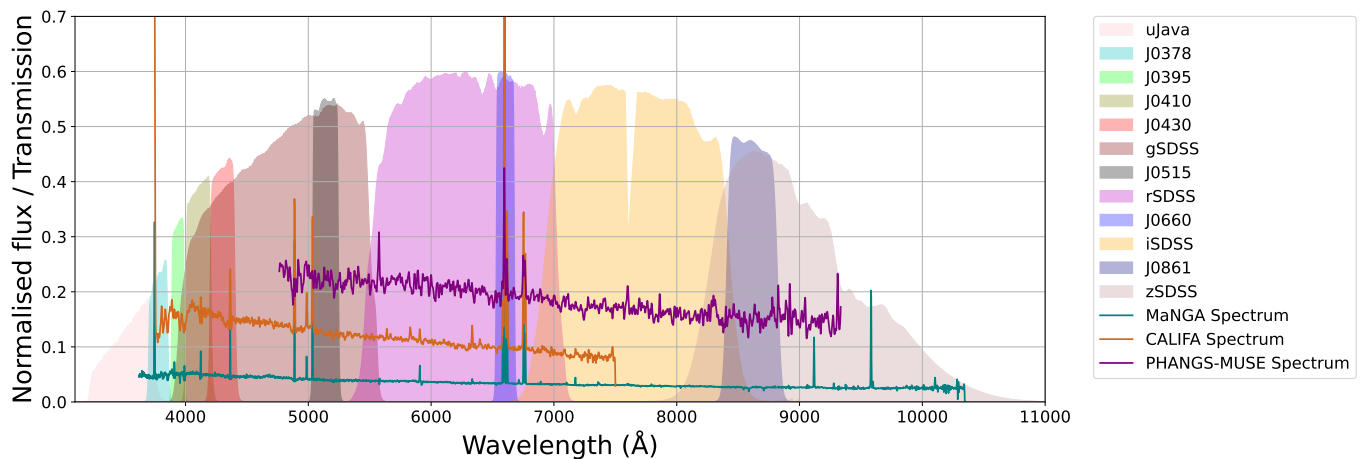


Fig. 2: The filter curves of J-PLUS compared to the spectra of PHANGS-MUSE (NGC1087 at 307, 457 xy position), CALIFA (NGC3395 spectra at 79, 72 xy position) and MaNGA (MaNGA–8150-6103 spectra at 26, 27 xy position).

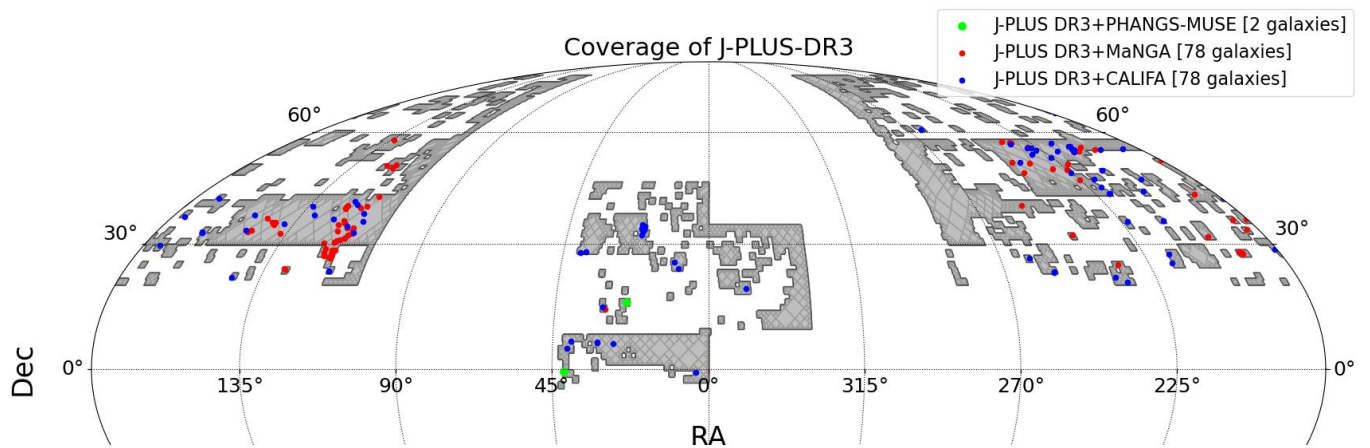


Fig. 3: Coverage of J-PLUS DR3 overplotted with distribution of cross matched catalogs of J-PLUS DR3 with PHANGS-MUSE, CALIFA and MaNGA.

PMAS/PPAK integral field spectrophotometer, mounted on the Calar Alto 3.5 m telescope. It utilises an hexagonal field-of-view (FoV) of $74'' \times 64''$. It has two observing modes: Intermediate spectral resolution (V1200, $R \sim 1550$) and low resolution (V500, $R \sim 850$). The CALIFA observations were carried out between 2010 and 2016.

We used version 2.3 from the extended data release (eDR) of CALIFA (Sánchez et al. 2023) that includes 895 galaxies. This version has significantly improved spatial resolution and image quality. The PSF is improved from ~ 2.4 arcsec to ~ 1 arcsec of FWHM. The configuration includes the low-resolution setup (V500, $R \sim 850$), integration time of 900 s per pointing, with a wavelength range of 3745 and 7500 Å. The spatial sampling of the eDR CALIFA data is $0.5''/\text{pixels}$ with a wavelength resolution of $2\text{Å}/\text{slice}$. The eCALIFA cubes are downloaded from the CALIFA website³. The downloaded CALIFA cubes are already corrected for Galactic extinction using the method by Schlegel et al. (1998) and Cardelli et al. (1989).

2.4. MaNGA

Mapping Nearby Galaxies at Apache Point Observatory (MaNGA; Bundy et al. 2015) is a program under the fourth phase of the Sloan Digital Sky Surveys (SDSS-IV; Blanton et al. 2017). MaNGA has mapped the kinematics and composition of 10,100 nearby galaxies in the redshift range of $0.01 < z < 0.15$ with an average of $z \sim 0.03$ using 17 hexagonal shaped IFUs mounted on Sloan Foundation 2.5m telescope at Apache Point Observatory from 2014 to 2020. The IFU size ranges from 12 arcsecs (19 fibers) diameter to 32 arcsecs (127 fibers) with a wavelength coverage of 3600 - 10000 Å across $\sim 2700 \text{ deg}^2$ and a spectral resolution of $R \sim 2000$. The medium spatial resolution of MaNGA is $\sim 2.54''$. The pixel scale of MaNGA is $0.5''/\text{pixel}$ with a wavelength resolution of $0.834 \text{ Å}/\text{slice}$. The MaNGA cubes are downloaded from DR17 archive⁴. The MaNGA fluxes are not corrected for Galactic extinction.

The comparison of the instrumental properties of MUSE, MaNGA, and CALIFA with J-PLUS is given in Table 2 and Figure 1 clearly demonstrate the capability of J-PLUS's wide field compared to these IFUs to cover the complete size of nearby

³ <https://ifs.astroscu.unam.mx>

⁴ https://data.sdss.org/sas/dr17/manga/spectro/redux/v3_1_1

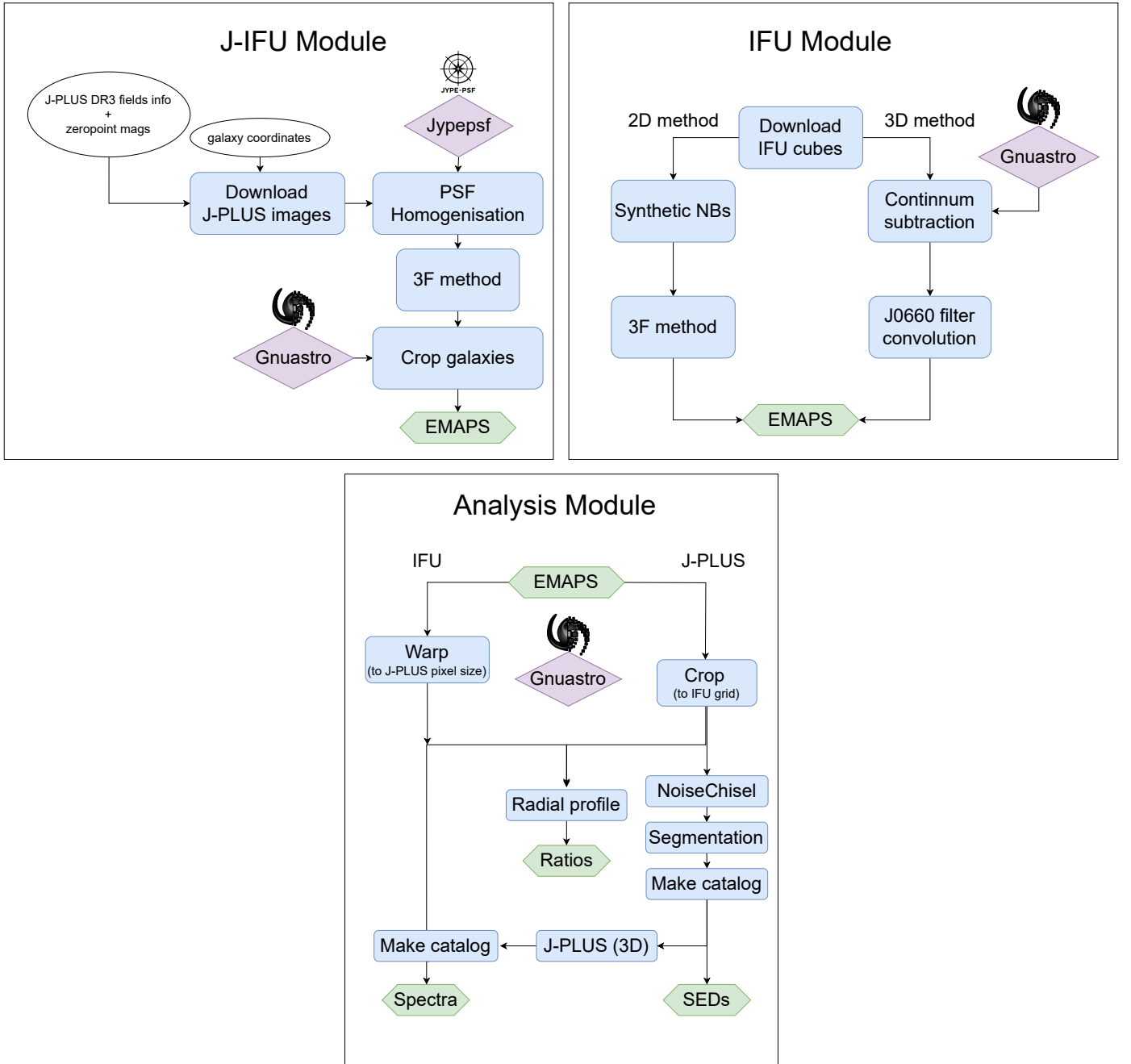


Fig. 4: Flowchart of the J-SHE modules. Top left: J-IFU module. Top right: IFU module. Bottom: Analysis module. White ellipses are inputs, purple blocks are external packages, blue boxes indicate different processes, and green hexagons represent outputs.

galaxies and their surrounding environment. Additionally, J-PLUS offers an advantage in wavelength coverage (compared to CALIFA and PHANGS), as illustrated in Fig. 2, which presents J-PLUS filter curves alongside spectra from PHANGS-MUSE (NGC1087), CALIFA (NGC3395), and MaNGA (MaNGA-8150-6103) galaxies for spectral coverage comparison.

3. Sample selection

The sample of nearby galaxies was selected from the J-PLUS DR3 survey at redshift of $z < 0.0165$ (or about 70 Mpc) based on the width ($\sim 140 \text{ \AA}$) of the $J0660$ filter centered at 6600 \AA (cov-

ering $H\alpha$ 6562.8 \AA). For the validation of our method of building the $H\alpha$ emaps with spectroscopy we selected a sample based on the cross-matched catalogs of MUSE-PHANGS, CALIFA, and MaNGA with J-PLUS DR3. Based on their IFU galaxy spectra, we have verified that the redshift range of all the selected galaxies ensures that the $H\alpha$ emission line is completely covered by this filter. The $[N \text{ II}]$ 6583 \AA line is outside the $J0660$ filter at $z > 0.014$.

Within PHANGS-MUSE, two galaxies overlap with J-PLUS DR3: NGC0628 at $z=0.0056$ and NGC1087 at $z=0.00219$. The full disk of the galaxy NGC 1087 has been observed in MUSE with 6 pointings, and the center of NGC 628 is observed in

MUSE with 12 pointings. The total exposure time of MUSE observation of NGC628 is 36750 seconds (10.2 hours) and 15957.46 seconds (4.4 hours) for NGC1087.

There are 176 galaxies cross-matched with J-PLUS DR3 and eCALIFA, with 78 galaxies in the redshift range of $z < 0.0165$. Among them, 20 galaxies are early-type (E/S0), 9 galaxies show dust-lane features, and 48 galaxies show clear evidence of star formation activity (based on GALEX-UV and $H\alpha + [\text{NII}]$ images) in the visual morphology and exhibit $H\alpha$ emission line at 6562.8 Å rest frame wavelength in CALIFA spectra. Among the 48 galaxies, the $[\text{NII}]\lambda 6583$ line lies outside the filter window for redshifts greater than 0.014 for 10 galaxies. Above redshifts greater than 0.0165, the $H\alpha$ line begins to fall outside the filter curve, and galaxies with such redshifts were excluded from the sample.

From the 10,000 MaNGA galaxies, 3,509 galaxies are in the J-PLUS DR3. Within a redshift range of $z < 0.0165$, the final cross-matched catalog amount to 78 J-PLUS-MaNGA galaxies. Among these, 65 galaxies have $H\alpha$ emission line (i.e., star-forming) in their MaNGA spectra and 13 galaxies do not show $H\alpha$ line. Seven galaxies are with the morphology of early type (E/S0). From the MaNGA spectra, we noticed that for 38 galaxies, the $[\text{NII}]$ line is partially or completely outside the filter curve at $z > 0.014$ and 30 galaxies have only the $H\alpha$ line within the filter curve, while the $[\text{NII}]$ line is completely outside the filter curve.

The total sample includes 158 galaxies with 3D data cubes from either of the aforementioned IFUs. For the final analysis, we used 115 galaxies that exhibit $H\alpha$ line in their spectra and have coverage of the full $H\alpha$ line within the J0660 filter curve. Fig. 3 shows the coverage of J-PLUS DR3 with the distribution of the final sample selected from the cross-matched catalog. The information of the final cross-matched sample is given in Appendix A.1.

4. The J-SHE Pipeline for building emaps of J-PLUS and IFUs

In this section, we describe the methodology followed to build the emaps and radial profile of galaxies, SEDs, and spectra of emission line regions from J-PLUS and IFUs. The J-PLUS Spatially-resolved $H\alpha$ Emission line (J-SHE) pipeline is written in GNU MAKE mainly utilizing GNU Astronomy Utilities (Gnuastro; Akhlaghi & Ichikawa 2015) and Python packages. Gnuastro is an official GNU package for the manipulation and analysis of astronomical data. Our pipeline consists of three modules (see Fig. 4). The first and second modules are dedicated to building emaps for J-PLUS (hereafter, J-IFU module) and IFUs (hereafter, IFU module) respectively. The third module generates the galaxy radial profiles, SEDs, and spectra of emission line regions from the emaps (hereafter, Analysis module).

4.1. J-IFU module

The J-IFU module builds the $H\alpha + [\text{NII}]$ emaps of J-PLUS galaxies. The input of the pipeline are the J-PLUS observation field tile information (tile id and zero points), and galaxy coordinates (RA and Dec). The initial step in the pipeline involves downloading the J-PLUS images of the tile in 12 filters that contain the requested galaxies. This is followed by PSF homogenisation on all images of the field. This process is done using JYPE-PSF, which is described in the next section. After the PSF homogenisation, we construct the emaps by following the recipe

of three filter (3F) method (see Sect. 4.1.3) from Vilella-Rojo et al. (2015). After building the emap of each J-PLUS observation field, we cropped the image to a small size by including the extent of the galaxy for further analysis. The flow chart of the module is given in Fig. 4 (top-left flowchart) and more details are described below.

4.1.1. PSF homogenization

JYPE-PSF is a Python module for PSF modeling, analysis, and normalization within the OAJ data reduction pipeline developed by the Department of Data Archival and Processing (DPAD) at the CEFCA. This module can perform an analysis of the 2D variations of the PSF of J-PLUS coadded images using SEXtractor (Bertin & Arnouts 1996) and PSFEx (Bertin 2011). PSFEx computes a space-varying kernel that transforms the PSF of an image into an arbitrary PSF. Each J-PLUS tile consists of 12 coadded images generated at the same position for each filter. This program is responsible for normalizing the 2D variations of the PSF of each tile to a target PSF.

JYPE-PSF first analyze the full width at half-maximum (FWHM) of the entire tile and select an optimal target PSF as the highest FWHM measure in that tile. Using PSFEx, it derives the PSF homogenization kernel for the input coadded images. Then the convolution kernel $K(x)$ is applied to the PSF model, and minimizes (based on χ^2) the difference with the target PSF for the entire tile. The homogenization kernel components are stored as a FITS data cube. The target shape is a perfectly round analytical function of the Moffat profile. Finally, each coadded image is convolved using Fast Fourier Transform (FFT) with this kernel to homogenize the variable PSF to a constant arbitrary shape to the target PSF.

4.1.2. Zero point map

There is a (X,Y) variation of the zero point with the position of the source on the CCD FoV for every J-PLUS observation. This observed variation can be influenced by several factors, including changes in airmass across the observation, scattered light in the focal plane, and positional dependencies in the effective filter transmission curves as discussed in López-Sanjuan et al. (2019, 2024), and references therein. It is not corrected in the final DR3 images and the correction is estimated in López-Sanjuan et al. (2019) with the following equation,

$$ZP = ZPT + A_CALIB \times X + B_CALIB \times Y + C_CALIB,$$

where the parameters A_CALIB, B_CALIB, and C_CALIB, define the position dependence of the zero point, which is downloaded from the J-PLUS database using ADQL. More details are given in López-Sanjuan et al. (2019). We applied this correction in the final flux calibration of emaps.

4.1.3. 3F method

In the 3F method (Vilella-Rojo et al. 2015), two broad-band filters (rSDSS and iSDSS in the case of $H\alpha$) are used to trace the continuum and one narrow-band filter ($H\alpha$ covering J0660) is used to trace the emission line. Then the $H\alpha + [\text{NII}]$ flux is derived using Eq.(3) from Vilella-Rojo et al. (2015) as shown below,

$$F_{H\alpha+[\text{NII}]} = \frac{(\bar{F}_{r'} - \bar{F}_{i'}) - \left(\frac{\alpha_r - \alpha_{i'}}{\alpha_{F660} - \alpha_{i'}}\right)(\bar{F}_{F660} - \bar{F}_{i'})}{\beta_{F660} \left(\frac{\alpha_r - \alpha_{i'}}{\alpha_{F660} - \alpha_{i'}}\right) + \beta_{r'}}$$

The \bar{F} values represent the observed average fluxes inside the filters, while α and β are defined as:

$$\alpha_x \equiv \frac{\int \lambda^2 P_x(\lambda) d\lambda}{\int P_x(\lambda) \lambda d\lambda}, \quad \beta_x \equiv \frac{\lambda_s P_x(\lambda = \lambda_s)}{\int P_x(\lambda) \lambda d\lambda},$$

where, $\lambda_s = \lambda_{H\alpha} = 6562.8 \text{ \AA}$.

Vilella-Rojo et al. (2015) have demonstrated that using two filters for continuum estimation provides a more accurate representation of the continuum's true shape compared to assuming a flat continuum with a single filter.

4.2. IFU module

The IFU module constructs the H α + [NII] emaps from other IFUs (here it is PHANGS-MUSE, CALIFA, and MaNGA) used for validation. The three data cubes are in different formats. The flowchart of this module is given in the upper right of Fig. 4. The initial step of the module is downloading the IFU cubes. We followed two different methods to build the IFU emaps for comparison.

In the first method (called "2D" in the flow chart), we initially build synthetic NBs from IFU cubes by convolving with J-PLUS filter curves. This creates rSDSS, iSDSS and J0660 synthetic images. Then, we followed the 3F method (as in the J-IFU module) for the continuum subtraction. For filter convolution, we use the MPDAF package of Python (Piqueras et al. 2019). It is a Python package used for the analysis of VLT/MUSE IFU cubes.

In the second method (called "3D" in the flow chart), we first estimate and subtract the continuum from the 3D cube and then convolve the continuum subtracted cube with the filter covering the emission line (e.g., J0660). For 3D continuum subtraction, we used Gnuastro: `astarithmetic` command. We estimate the continuum flux at every slice of the IFU cube by taking the sigma-clipped median value of $N/2$ ($N=100$) slices or wavelength steps before and after it. The steps are given in the section of continuum subtraction in the Gnuastro reference manual (Akhlaghi 2024). After the 3D continuum subtraction, the 3D cube is collapsed to a 2D image by convolving the cube with the J0660 filter transmission curve.

After constructing emaps, the 2D images from the IFUs are warped to the pixel grid of the J-PLUS image of the galaxy using `astwarp` from Gnuastro. The warping pixel scale is set by the highest pixel scale size among the IFUs and J-PLUS. The one with the highest pixel scale size will be used to re-scale the other. PHANGS-MUSE (0.2"/pixel), CALIFA (0.5"/pixel) and MaNGA (0.5"/pixel) have higher spatial sampling compared to J-PLUS (0.55"/pixel), thus the pixel scale of the IFUs are changed to J-PLUS size. Afterwards, the image size of J-PLUS is resampled to the same image size of IFUs. This step is necessary for the pixel-to-pixel comparison between the emaps as we do in later sections.

The examples of output 2D emaps from these two modules and their comparison are given from Figures 5 to 7. The figures also show the full extent of the galaxy emap and the cropped images based on the IFU size. The size of the IFU FoV is labelled in the figure.

4.3. Analysis module

The analysis module produces the radial profile from galaxy emaps (see Sect.4.3.1) identifies and constructs the SEDs and

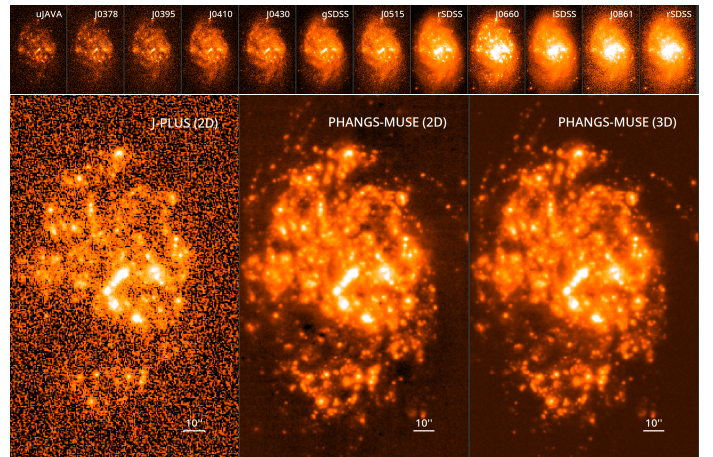


Fig. 5: H α + [NII] emap of NGC 1087 in J-PLUS and in PHANGS-MUSE (2x3 MUSE pointings) constructed in Sect. 4.1 and Sect. 4.2. The J-PLUS images in 12 filters are shown in the top panel, plotted with the same surface brightness level.

spectra of emission line regions (see Sect.4.3.2). We extensively used Gnuastro packages inside this module for analysis.

4.3.1. Estimation of the radial profiles

The warped emaps are used to plot radial profiles of galaxies. We use Gnuastro's `astscript-radial-profile` (Infante-Sainz et al. 2024) for this step. We estimated the axis ratio and position angle of the galaxies from rSDSS images using Gnuastro's `MakeCatalog`, `astmkcatalog` (Akhlaghi 2019b). Then the final estimation of these parameters was based on the shape of H α + [NII] images. For MaNGA images, we used the circular aperture because of their small image size.

We show some examples of radial profile of J-PLUS galaxies in comparison from MUSE (Fig. 8), CALIFA (Fig. 9) and MaNGA (Fig. 10). The upper panels are the emaps and their radial profiles are given in the middle panels. We discuss the main results from this comparison in Sect. 5.

4.3.2. Clump detection and SEDs

Here we discuss the steps for the identification and SED construction of the emission line regions. `NoiseChisel` and `Segment` (Akhlaghi & Ichikawa 2015; Akhlaghi 2019a) of Gnuastro are good tools for identifying the emission line regions in galaxies. `NoiseChisel` is used to separate the signals from the noise and estimate the background of the images. The sky-subtracted images are then used to identify the emission line regions in the galaxies using Gnuastro's `astsegment` program (Akhlaghi 2019a). It finds significant (compared to the ambient noise) local maxima over a region that is already detected to have a signal. `astsegment` works by growing pixels around the local maxima until the local minima are reached. Therefore, it is able to trace the shape of star-forming clumps accurately without any parametric assumptions. For more, see Section 3.2 of Akhlaghi & Ichikawa (2015) and Section 3 of Akhlaghi (2019a).

The segmentation map output provides the pixels associated to each clump. Using the position and area of the clumps detected from the J-PLUS H α emaps, we measured the total

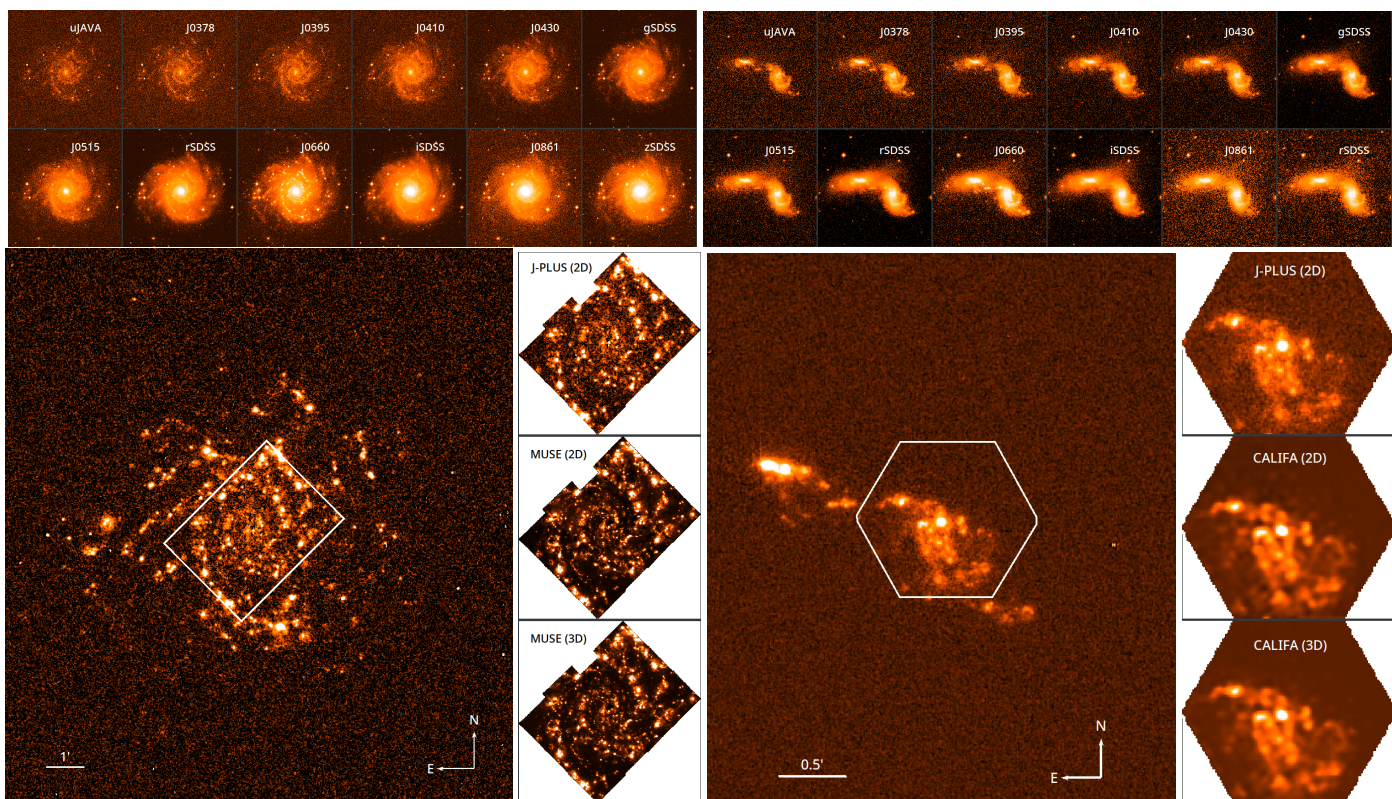


Fig. 6: top: J-PLUS images in 12 filters. left: Full extent of $H\alpha$ + $[NII]$ emap of NGC 628 in visible in a crop of the J-PLUS tile with a label of PHANGS-MUSE coadd size (consisting of 3x4 MUSE pointings; white square) of same galaxy, and emaps constructed in Sect. 4.1 and Sect. 4.2. Right: Full extent of $H\alpha$ + $[NII]$ emap of NGC 3395 in J-PLUS with a label of CALIFA FoV (white), and emaps constructed in Sect. 4.1 and Sect. 4.2

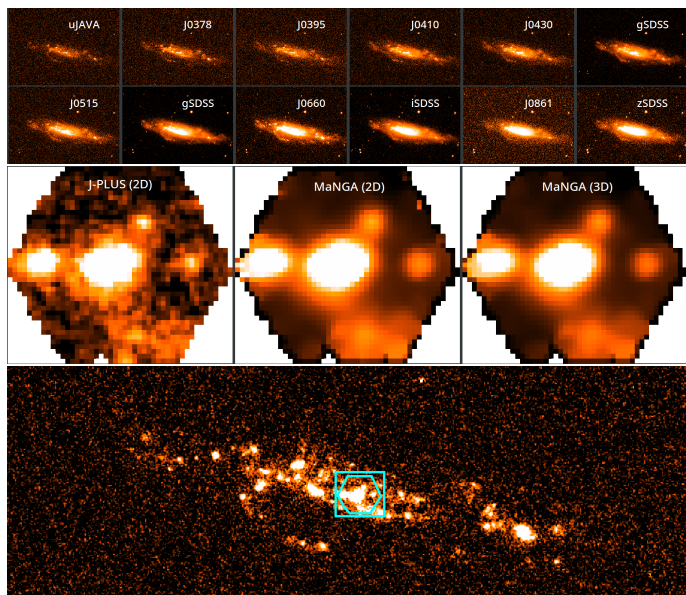


Fig. 7: Top: J-PLUS images in 12 filters. Middle: Comparison of J-PLUS emap with MaNGA emaps constructed in different methods. Lower: Full extent of $H\alpha$ + $[NII]$ emap of MaNGA-8150-6103 in J-PLUS with a label of MaNGA FoV (blue)

fluxes of clumps in all 12 filters for constructing their SEDs. `astmkcatalog` is used for making the catalog of the detected

clumps from $H\alpha$ + $[NII]$ map in 12 filters. Then the SEDs are constructed using the fluxes from 12 filters.

Similarly, for getting the IFU spectra of the emission line regions detected in J-PLUS emaps, we used the same clump labeled images. For this, we first create a 3D cube of the segmentation map of J-PLUS with the same 3rd axis size in IFUs. Then using the Gnuastro's `MakeCatalog`, we measured the spectra catalog of all clumps. Then we compared the SEDs and the IFU spectra of every clump.

The SEDs and IFU spectra of some emission line regions of different galaxies are given from Fig. 11 to Fig. 13. CALIFA cubes are already corrected for galactic extinction. Therefore, we have applied the galactic extinction correction for J-PLUS images using attenuation values in each filter (López-Sanjuan et al. 2019) downloaded from J-PLUS the database. The extinction coefficients in J-PLUS were based on the recalibration of Schlafly & Finkbeiner (2011) on Schlegel et al. (1998) maps. We removed this recalibration correction by multiplying the J-PLUS extinction coefficients by 1.16 to match the CALIFA extinction (see Schlafly & Finkbeiner 2011 for more details).

5. Results and discussions

5.1. Comparison of $H\alpha$ + $[NII]$ emaps of J-PLUS with other IFUs

The spatially resolved $H\alpha$ maps trace the star formation at < 10 Myr, ionization mechanisms, mass assembly, and other galaxy properties. The precise continuum subtraction is essential for creating emaps that accurately estimate these physical proper-

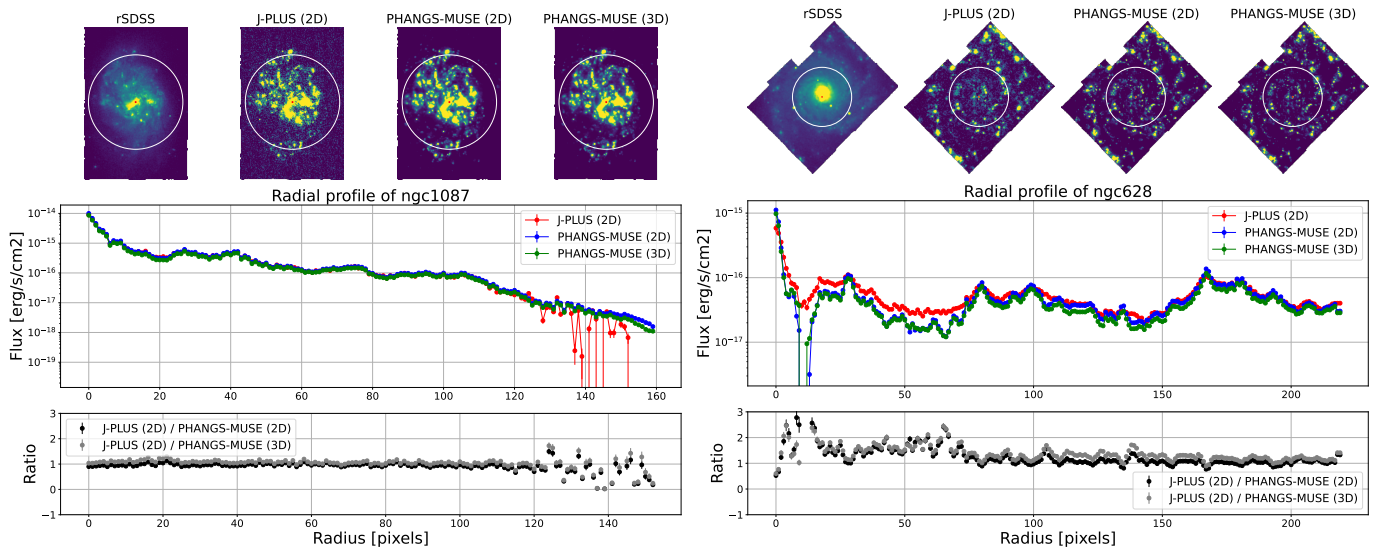


Fig. 8: Upper: rSDSS (J-PLUS), J-PLUS (2D), PHANGS-MUSE (2D) and PHANGS-MUSE (3D) $H\alpha$ + $[NII]$ map images of NGC 1087 (left) and NGC 628 (Right). White circle is in 100 pixels radius. Middle: Radial profiles of J-PLUS (2D), PHANGS-MUSE (2D) and PHANGS-MUSE (3D) $H\alpha$ maps. Lower: The ratio of the radial profiles J-PLUS (2D)/PHANGS-MUSE (3D). The center and radius of 100 pixels are labeled with red and white circles respectively. Note that emaps are in the same flux scale except rSDSS.

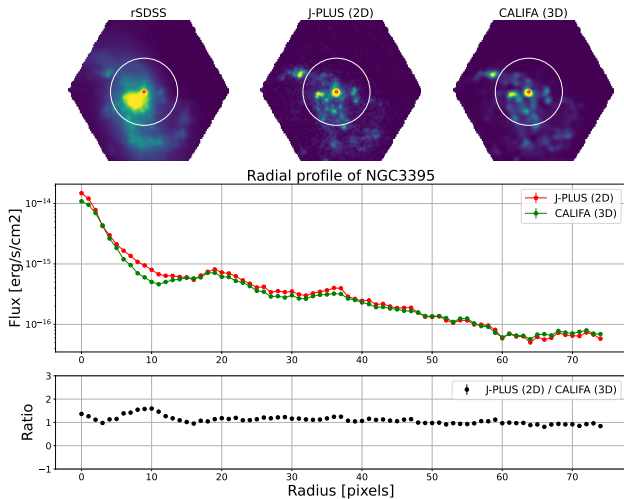


Fig. 9: Upper: rSDSS (J-PLUS), J-PLUS (2D), and CALIFA (3D) $H\alpha$ + $[NII]$ map images of NGC 3395 (White circle is in 30 pixels radius). Middle: Radial profiles of J-PLUS (2D), and CALIFA (3D) $H\alpha$ maps. Lower: The ratio of the radial profiles J-PLUS (2D)/CALIFA (3D). Note that emaps are in the same scale except rSDSS.

ties of the observed regions. Here we discuss our findings from the comparison of the $H\alpha$ maps constructed from J-SHE pipeline with the other IFUs.

5.1.1. PHANGS-MUSE emaps

For the validation with PHANGS-MUSE, the two spiral galaxies that overlap with J-PLUS DR3 are used. Their $H\alpha$ + $[NII]$ map shows a smooth and continuous $H\alpha$ emission (Fig. 8) and the star-forming regions are mostly distributed along the spiral arms. The radial profiles of NGC 1087 from J-PLUS and PHANGS-MUSE demonstrate that the 3F method effectively reproduces emaps comparable to those derived from PHANGS-

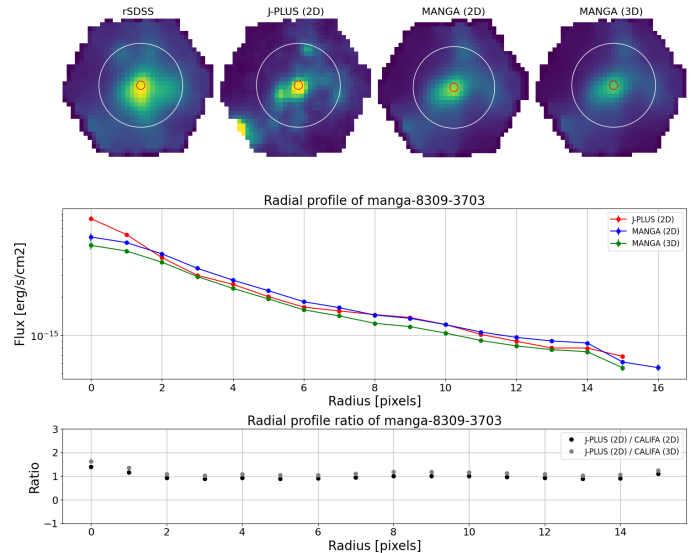


Fig. 10: Upper: rSDSS, J-PLUS (2D), MaNGA (2D) and MaNGA (3D) $H\alpha$ map images of MaNGA-8309-3703 (White circle is in 10 pixels radius). Middle: Radial profiles of J-PLUS (2D), MaNGA (2D) and MaNGA (3D) $H\alpha$ + $[NII]$ maps. Lower: The ratio of the radial profiles J-PLUS (2D)/MaNGA (2D). Note that emaps are in the same scale except rSDSS.

MUSE. However, in the case of NGC 628, the flux in the cube is slightly lower compared to J-PLUS, possibly due to the over-subtraction of the sky in the PHANGS-MUSE observation of NGC 628 (Emsellem et al. 2022). This is because the NGC628 coadd is fully covered by the central part of the galaxy and does not have any pixels from outside of the galaxy's main disk. This problem did not occur for NGC1087 because the MUSE coadd extended sufficiently outside of the main disk to allow accurate estimation of the sky level. Also in the MUSE-PHANGS data, there is a significant drop in the flux near the center of NGC628 (near $R \sim 20$ pixels), in contrast with the J-PLUS data and clearly

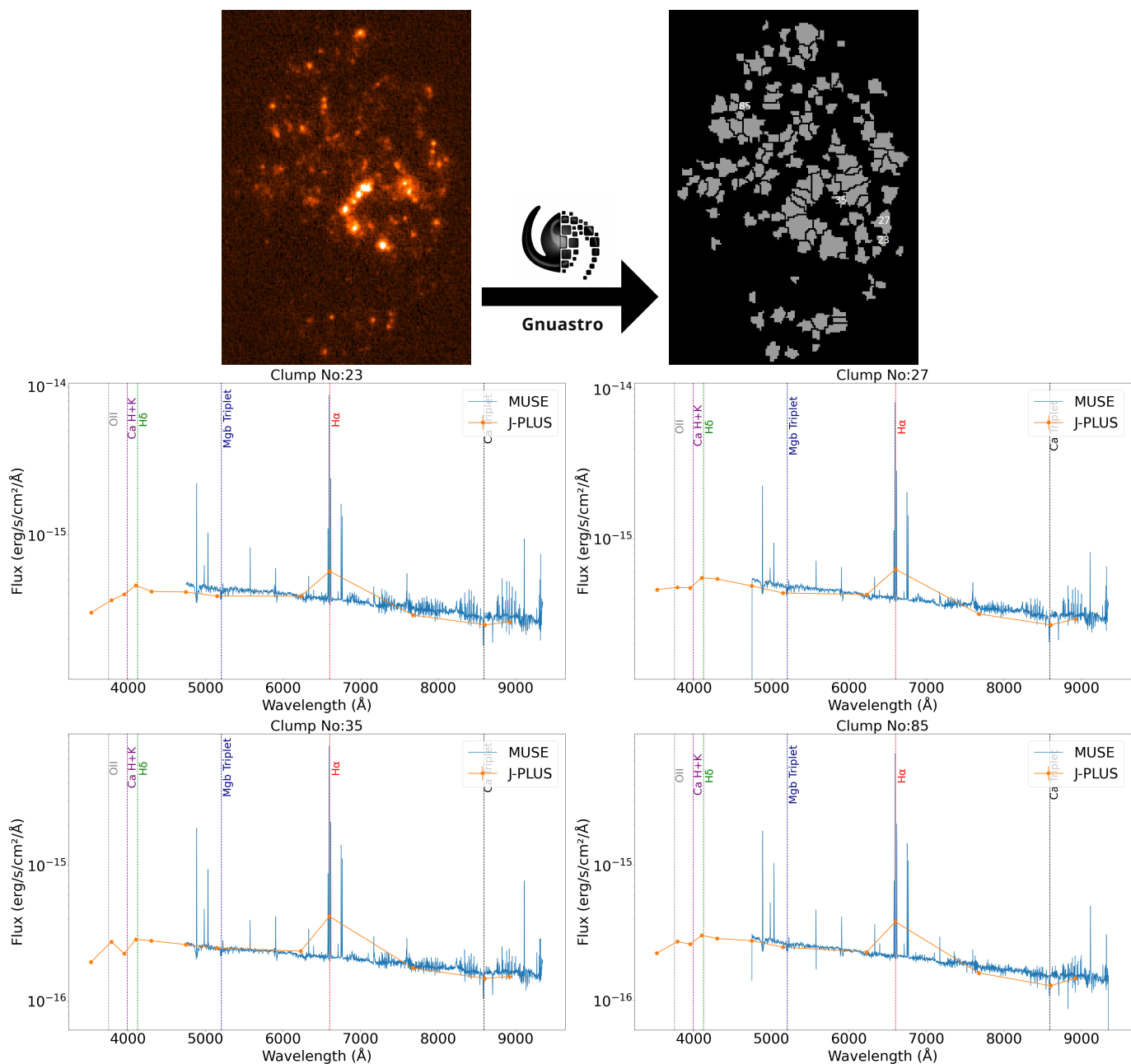


Fig. 11: Top: $H\alpha$ + $[NII]$ map and segmentation map of NGC 1087, Bottom: Examples of photospectra from J-PLUS in comparison with MUSE spectra of the clumps.

indicates over subtraction due to an artifact arising from a bright star near the center of the galaxy.

5.1.2. CALIFA emaps

In the CALIFA sample, galaxies have different morphological types. The wavelength coverage of CALIFA only covered a part of the iSDSS filter, 64% of the iSDSS J-PLUS filter curve is beyond the edge of the CALIFA wavelength range (see Fig. 2). Therefore, we only used the CALIFA emap from the 3D method to validate the J-PLUS emaps. The $H\alpha$ + $[NII]$ map shows that CALIFA galaxies exhibit different features of $H\alpha$ + $[NII]$ emission, which can be observed along the rings, within spiral arms, and as clumpy structures. From Fig. 6 and in Appendix Fig. B.1 we show emaps of some star-forming CALIFA galaxies.

5.1.3. MaNGA emaps

MaNGA provides high-spectral resolution with a larger spectral coverage for individual galaxies but covers a smaller FoV compared to other IFUs studied here. Due to its smaller field of view at the redshift range studied here, most of the MaNGA observations cover the center of galaxies or part of the galaxy regions. Fig. 7 clearly shows the advantage of J-PLUS FoV compared to that of MaNGA. For this case, J-PLUS can provide the spatially resolved $H\alpha$ structure of the full extent of the galaxy in a single observation, while MaNGA only covers the central region of this galaxy. We have demonstrated emap comparison of some of the MaNGA galaxies in Fig. B.2.

Note that the cases where the absorption present within the filter windows affects the estimation of the emap and the flux will be underestimated.

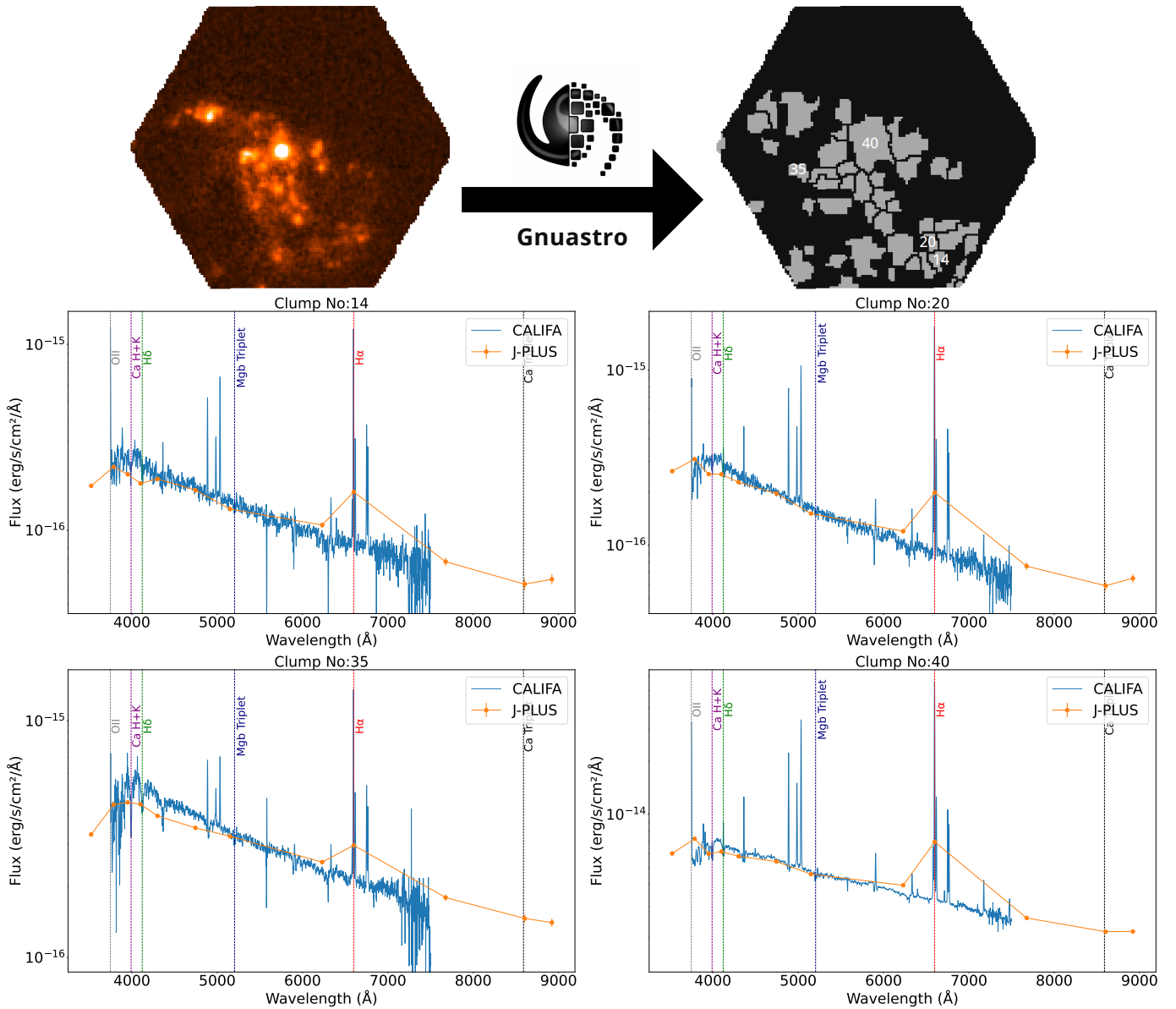


Fig. 12: Top: H α + [NII] map and segmentation map of NGC 3395 (only the part of CALIFA size), Bottom: Examples of J-PLUS SEDs in comparison with CALIFA spectra of the clumps

5.2. Radial profile flux ratios

The ratio of J-PLUS to IFU emap radial profile can help in identifying regions of significant divergence and provides a straightforward way to compare the two emaps. This can reveal if one method consistently overestimates or underestimates a measurement. A ratio close to 1 indicates good agreement between the two methods and values significantly different from 1 suggest discrepancies. Here we have analyzed how the radial profile ratios vary with radius. We have plotted the ratio of the J-PLUS (2D) profile to the IFUs profile in the lower panel of Fig. 8 to Fig. 10.

The variation in the radial profile of a given galaxy obtained from different instruments can indeed be influenced by several factors. Instruments may have different background noise levels, different levels of sensitivity, depths, and different PSFs. In the comparison of PHANGS-MUSE with J-PLUS, the radial profile ratios of NGC1087 (left panel in Fig. 8) show that the values are consistently close to 1 in the two methods, suggesting that both

methods yield similar results. But for NGC 628 (right panel in Fig. 8), the discrepancy is due to the difference in the sky subtraction (see sect.5.1.1). Background noise can introduce large scatter in the radial profile ratios.

The scatter in the ratio profile also depends on the morphology. The spiral galaxies with continuous H α emission show strong agreement and a ratio of one in the radial profile in two different instruments. Galaxies with a clumpy or ring structure show some discrepancy in the region where there is very low flux because of the different background contribution, which leads to a large scatter in the ratio of radial profiles. For example, for CALIFA galaxies, (e.g., NGC2780, UGC03899, and NGC3600) in the appendix: Fig. B.1 show a large scatter in the ratios, where there is less S/N. The ratio of the profile with high S/N shows values close to one with a maximum scatter of ~ 0.2 dex.

We also noticed that the galaxies hosting AGN at the center (e.g., NGC 5443) show a variation in the flux at the center in J-PLUS (high) compared to CALIFA. This might be due to

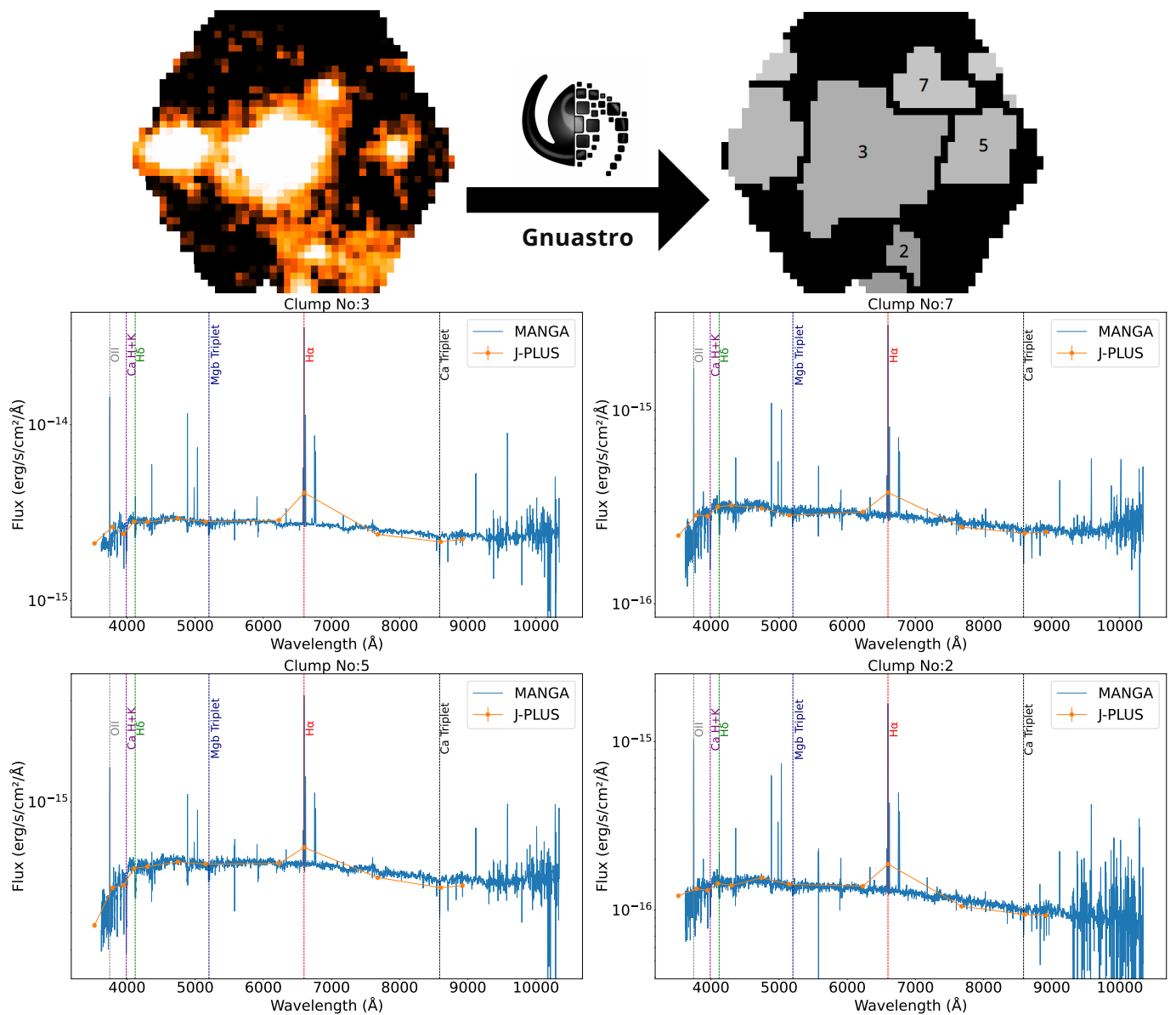


Fig. 13: Top: $H\alpha$ + $[NII]$ map and segmentation map of MaNGA-8150-6103, Bottom: Examples of J-PLUS SEDs in comparison with MANGA spectra of the clumps.

the optical variability of AGN and that the surveys were not observed at the same time.

5.3. $H\alpha$ emission line regions

The $H\alpha$ emission line is crucial to identify the star-forming regions and estimate their star formation rates. The SEDs of these spatially resolved star-forming regions help us to investigate the stellar population within galaxies, and their properties like age, metallicity, and luminosity provide insights into the evolution in galaxies. Because J-PLUS is a large-area photometric survey, it provides an efficient way to map spatially resolved star-forming regions in a large sample of galaxies, offering an alternative to spectroscopy, which is more time consuming. In order to validate our method of building J-PLUS SEDs of $H\alpha$ emission line regions, we have compared the SEDs with the spectra from IFUs discussed in Section 2. Later we are planning to fit the SEDs of these clumps to study the stellar population properties.

5.3.1. Comparing J-PLUS SEDs with IFU spectra

The upper panels of Figure 11 show the $H\alpha$ + $[NII]$ map and the Gnuastro clump map of PHANGS-MUSE NGC 1087, while the lower panel shows the SEDs and IFU-spectra of some examples of emission line (mostly star-forming) regions. We have detected 108 clumps in this galaxy. The J-PLUS SEDs and the PHANGS-MUSE spectra show good agreement. The emission lines are clearly visible in the SEDs.

The example for the CALIFA galaxy NGC 3395 is given in Fig. 12. In CALIFA, some of the clumps show a slight variation in the blue part, probably due to the difference of Galactic extinction correction and also due to the offset in astrometry. The clumps in PHANGS-MUSE and MaNGA (Fig. 13) show a perfect match between the spectra and SEDs. Although PHANGS-MUSE and CALIFA have higher spectral resolution, the advantage of J-PLUS is the wide spectral coverage. Compared to PHANGS-MUSE, J-PLUS has extended wavelength coverage in the blue part of the spectra, which mainly has a Ca + H + K 3970

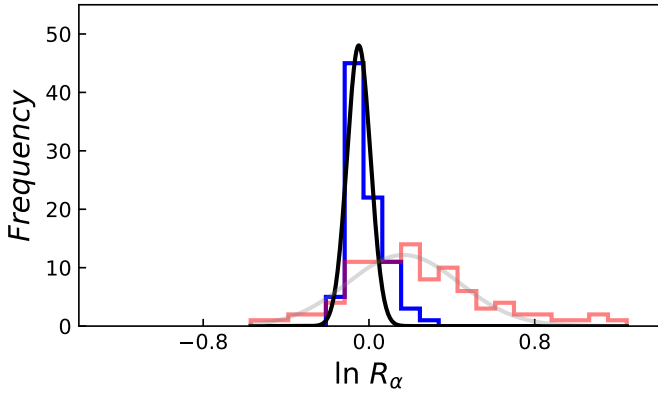


Fig. 14: The distribution of ratio of H α flux (with Gaussian fit) of emission line regions in J-PLUS to MUSE-PHANGS (blue) and MaNGA (red) IFUs.

\AA absorption line, OII 3727 \AA emission-line doublet. On the other hand, compared to CALIFA, J-PLUS has a wider wavelength coverage in the redder part of the spectra, including the Ca Triplet 8544.44 \AA . J-PLUS has similar spectral coverage as MANGA and shows strong agreement between the SED and the spectra of the clumps.

5.3.2. Ratio of J-PLUS and IFU H α + [NII] fluxes

To quantify the goodness of our extraction method, we analyzed the ratio of the J-PLUS and IFU H α + [NII] fluxes of detected emission line clumps, noted R_α . IFU emaps created from pseudo J-PLUS NBs (2D method) is used for this analysis.

For PHANGS-MUSE, we used 108 clumps detected in NGC 1087. We chose to analyze only NGC 1087 due to the over-subtraction of the sky in NGC 628, which will affect the reliability of the final results. We only consider clumps with S/N greater than 10 to avoid low signal to noise areas. Fig. 14 shows the histogram of logarithm of R_α for 87 high-quality clumps detected in NGC1087 (blue). The median value of the Gaussian fit is -0.04 .

We also computed the ratio from the r -band fluxes of the clumps, finding a similar difference between J-PLUS and PHANGS-MUSE as in the H α flux ratios (Fig. 14). The r -band ratio, noted R_r , encodes a variety of observational differences between both datasets, such as flux calibration, sky subtraction, or effective FWHM. We corrected these effects in the H α ratio by just dividing each clump value with its r -band ratio, obtaining a normalized H α ratio (\bar{R}_α). The distribution of $\ln \bar{R}_\alpha$, which is a proxy for fractional differences, is presented in Fig. 15 (upper panel). We find a much better agreement between both datasets, with a median value of 0.02. We fitted a Gaussian function to the distribution, finding $\ln \bar{R}_\alpha = 0.02 \pm 0.07$. That denotes that J-PLUS is recovering the H α flux with 2% bias and 7% dispersion. We also plotted $\ln \bar{R}_\alpha$ with S/N of the clumps. The scatter is more for lower S/N clumps than for higher S/N clumps.

In the case of MaNGA, a small part of each galaxy is covered and a few star-forming regions are detected. For the complete sample of MaNGA galaxies, we have detected a total of 169 clumps. Again, we discarded the clumps with S/N less than 10 and also removed those detected in J-PLUS and not present in MaNGA. Explanation for those cases are beyond the scope of this paper. A more detailed study of these clumps will be discussed in a forthcoming article. The red histogram in

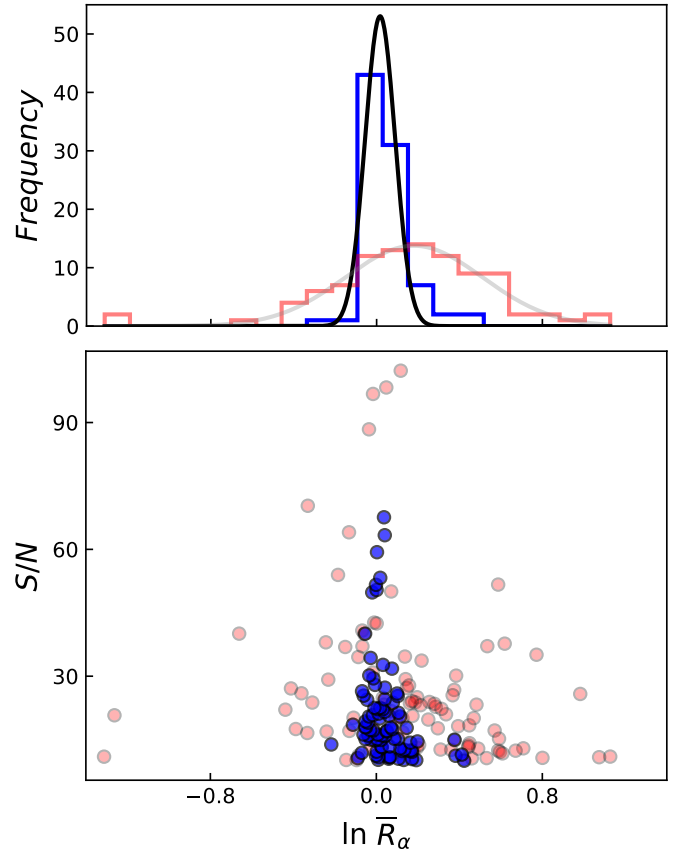


Fig. 15: Upper: The distribution of $\ln \bar{R}_\alpha$ with Gaussian fit for MUSE-PHANGS (blue) and MaNGA (red). Lower: $\ln \bar{R}_\alpha$ vs S/N plot for MUSE-PHANGS (blue) and MaNGA (red) emission line regions.

Fig. 14 shows the distribution of R_α , with a Gaussian fit yielding $\ln R_\alpha = 0.16 \pm 0.27$. After normalizing by the r -ratio, the resulting value of $\ln \bar{R}_\alpha$ value is 0.18 ± 0.33 . We also calculated the ratios of the i and J0660 filters between J-PLUS and the synthetic J-PLUS filters from MaNGA, obtaining fitting values of 0.02 ± 0.11 , 0.04 ± 0.10 and 0.00 ± 0.14 respectively. The difference in continuum subtracted H α fluxes is expected due to the different PSFs between J-PLUS (1.1") and MaNGA (2.5"). The much larger MaNGA PSF FWHM is due to the hexagonal grid of optical fiber configuration (2"-core diameter fibers separated by 0.5") of the MaNGA survey which introduce systematic errors and underestimations of the flux measurements.

Since 2D emaps are not created for CALIFA due to incomplete coverage of the iSDSS filter's wavelength range, we exclude them from this analysis. Also, there is a slight difference in astrometry in CALIFA galaxies compared to the J-PLUS. We also noticed that there are some clumps that is detected in J-plus and not present in the CALIFA. Some of these were supernovae, which is already reported. The investigation of these objects are beyond the scope of this study. In future paper we will discuss more detail about the clumps in J-PLUS galaxies with their physics.

6. Conclusions

In this study, we developed and validated the J-SHE pipeline for constructing spatially resolved H α + [NII] emission maps and

extract the SEDs of every emission line region in nearby galaxies ($z < 0.0165$) in J-PLUS DR3 in a very automated way.

The main findings drawn from our study are summarized below.

- The wide FoV, spatial resolution, wavelength coverage, and narrow-band filters of J-PLUS are suitable for spatially resolved spectral studies of nearby galaxies.
- Emaps of $H\alpha+[NII]$ were derived using two filters to trace the continuum (r and i) and one to trace the emission line ($J0660$). The methodology was validated with 158 galaxies in common with the PHANGS-MUSE, CALIFA, and MaNGA IFU surveys.
- The J-PLUS emaps provide similar emission line regions and radial profiles when compared to the IFU surveys when analyzed using synthetic photometry to compute the J-PLUS extraction procedure.
- The $H\alpha+[NII]$ images from J-PLUS allowed us to extract photospectra for the star-forming clumps in the studied galaxy disks and their properties. This is less time-consuming as compared to spectroscopic surveys and can provide the SEDs of all the clumps within the wide field of view.
- The J-PLUS narrow bands cover key spectral lines such as $[OII]3727\text{\AA}$, Ca H+K, $H\alpha$, Ca triplet, and $[OIII]4959,5007\text{\AA}$ ($z>0.006$) providing valuable insights into various stages of stellar evolution and star formation processes in galaxies in resolved scales. The J-PLUS SEDs of the emission line regions clearly showcase these spectral features, mirroring the spectra extracted from IFU data in the same regions.
- The uniqueness of J-PLUS in comparison to other IFUs, is large FoV that allows us to map the complete extent of galaxy structure, galaxy interactions, galaxy groups, and galaxy clusters in a single FoV. J-Surveys can capture this wider contexts, providing insights into large-scale structures and galaxy interactions. This broader coverage can be advantageous for studying the global properties of galaxies and their environments.
- The measured $H\alpha+[NII]$ fluxes in the star-forming clumps from J-PLUS and the IFU data show a difference of 2% and a dispersion of 7% after correcting by differences in r-band. This validates the extraction and measurement procedures.

In subsequent papers, we will also provide the catalog of the SED information of all emission line regions in all nearby galaxies observed in J-PLUS DR3. This will help to study the spatially resolved stellar population and emission line properties of galaxies in statistical way. In the next project, we derive the resolved star formation main sequence using all the nearby galaxies having the spectroscopic redshift.

As a final note, the Javalambre Physics of the Accelerating Universe Astrophysical Survey (J-PAS; Benitez et al. 2014; Dupke et al. 2016) will observe thousands of square degrees in the northern sky and will provide data for thousands of galaxies with significantly improved spatial resolution thanks to its 56 narrow-band filters in the optical. Its continuous set of filters functions like a low-resolution IFU over large areas, enabling a deeper understanding of galaxy formation and evolution on resolved scales.

Acknowledgements. RPT thanks the Spanish Ministry of Science and Innovation (MCIN/AEI/10.13039/501100011033 y FEDER, Una manera de hacer Europa) with grant No. PID2021-124918NA-C43, the Governments of Spain and Aragón through their general budgets and the Fondo de Inversiones de Teruel. RPT also thanks the European Union - NextGenerationEU through the Recovery and Resilience Facility program Planes Complementarios con

las CCAA de Astrofísica y Física de Altas Energías - LA4. RPT acknowledge David Fernández Gil and Francisco Arizo Borillo for their valuable inputs during the analysis of this work. ACS acknowledges funding from the Brazilian agencies *Conselho Nacional de Desenvolvimento Científico e Tecnológico* (CNPq) and the Rio Grande do Sul Research Foundation (FAPERGS) through grants CNPq-314301/2021-6, FAPERGS- 24/2551-0001548-5. AE acknowledges the financial support from the Spanish Ministry of Science and Innovation and the European Union - NextGenerationEU through the Recovery and Resilience Facility project ICTS-MRR-2021-03-CEFCA. AAC acknowledges financial support from the Severo Ochoa grant CEX2021- 001131-S funded by MCIN/AEI/10.13039/501100011033 and the Spanish project PID2023-153123NB-I00, funded by MCIN/AEI. Based on observations made with the JAST80 telescope and T80Cam camera for the J-PLUS project at the Observatorio Astrofísico de Javalambre (OAJ), in Teruel, owned, managed, and operated by the Centro de Estudios de Física del Cosmos de Aragón (CEFCA). We acknowledge the OAJ Data Processing and Archiving Unit (UPAD) for reducing the OAJ data used in this work. Funding for the J-PLUS Project has been provided by the Governments of Spain and Aragón through the Fondo de Inversiones de Teruel; the Aragonese Government through the Research Groups E96, E103, E16_17R, E16_20R, and E16_23R; the Spanish Ministry of Science and Innovation (MCIN/AEI/10.13039/501100011033 y FEDER, Una manera de hacer Europa) with grants PID2021-124918NB-C41, PID2021-124918NB-C42, PID2021-124918NA-C43, and PID2021-124918NB-C44; the Spanish Ministry of Science, Innovation and Universities (MCIU/AEI/FEDER, UE) with grants PGC2018-097585-B-C21 and PGC2018-097585-B-C22; the Spanish Ministry of Economy and Competitiveness (MINECO) under AYA2015-66211-C2-1-P, AYA2015-66211-C2-2, AYA2012-30789, and ICTS-2009-14; and European FEDER funding (FCDD10-4E-867, FCDD13-4E-2685). The Brazilian agencies FINEP, FAPESP, and the National Observatory of Brazil have also contributed to this project. This work was partly done using GNU Astronomy Utilities (Gnuastro, ascl.net/1801.009) version 0.23.11-45775. Work on Gnuastro has been funded by the Japanese Ministry of Education, Culture, Sports, Science, and Technology (MEXT) scholarship and its Grant-in-Aid for Scientific Research (21244012, 24253003), the European Research Council (ERC) advanced grant 339659-MUSICOS, the Spanish Ministry of Economy and Competitiveness (MINECO, grant number AYA2016-76219-P) and the NextGenerationEU grant through the Recovery and Resilience Facility project ICTS-MRR-2021-03-CEFCA. This work was carried out as part of the PHANGS-MUSE collaboration. Based on observations collected at the European Southern Observatory under ESO programmes 1100.B-0651, 095.C-0473, and 094.C-0623 (PHANGS-MUSE; PI Schinnerer), as well as 094.B-0321 (MAGNUM; PI Marconi), 099.B-0242, 0100.B- 0116, 098.B-0551 (MAD; PI Carollo) and 097.B-0640 (TIMER; PI Gadotti). This study uses data provided by the Calar Alto Legacy Integral Field Area (CALIFA) survey (<http://califa.caha.es/>). Based on observations collected at the Centro Astronómico Hispano Alemán (CAHA) at Calar Alto, operated jointly by the Max-Planck-Institut für Astronomie and the Instituto de Astrofísica de Andalucía (CSIC). Funding for the Sloan Digital Sky Survey IV has been provided by the Alfred P. Sloan Foundation, the U.S. Department of Energy Office of Science, and the Participating Institutions. SDSS-IV acknowledges support and resources from the Center for High Performance Computing at the University of Utah. The SDSS website is www.sdss4.org. SDSS-IV is managed by the Astrophysical Research Consortium for the Participating Institutions of the SDSS Collaboration including the Brazilian Participation Group, the Carnegie Institution for Science, Carnegie Mellon University, Center for Astrophysics Harvard & Smithsonian, the Chilean Participation Group, the French Participation Group, Instituto de Astrofísica de Canarias, The Johns Hopkins University, Kavli Institute for the Physics and Mathematics of the Universe (IPMU) / University of Tokyo, the Korean Participation Group, Lawrence Berkeley National Laboratory, Leibniz Institut für Astrophysik Potsdam (AIP), Max-Planck-Institut für Astronomie (MPIA Heidelberg), Max-Planck-Institut für Astrophysik (MPA Garching), Max-Planck-Institut für Extraterrestrische Physik (MPE), National Astronomical Observatories of China, New Mexico State University, New York University, University of Notre Dame, Observatório Nacional / MCTI, The Ohio State University, Pennsylvania State University, Shanghai Astronomical Observatory, United Kingdom Participation Group, Universidad Nacional Autónoma de México, University of Arizona, University of Colorado Boulder, University of Oxford, University of Portsmouth, University of Utah, University of Virginia, University of Washington, University of Wisconsin, Vanderbilt University, and Yale University.

References

- Akhlaghi, M. 2019a, arXiv e-prints, arXiv:1909.11230
- Akhlaghi, M. 2019b, in *Astronomical Society of the Pacific Conference Series*, Vol. 521, *Astronomical Data Analysis Software and Systems XXVI*, ed. M. Molinaro, K. Shorridge, & F. Pasian, 299

- Akhlaghi, M. 2024, GNU Astronomy Utilities manual version 0.23, DOI:10.5281/zenodo.12738457 (Free Software Foundation)
- Akhlaghi, M. & Ichikawa, T. 2015, *ApJS*, 220, 1
- Bacon, R., Accardo, M., Adjali, L., et al. 2010, in *Society of Photo-Optical Instrumentation Engineers (SPIE) Conference Series*, Vol. 7735, *Ground-based and Airborne Instrumentation for Astronomy III*, ed. I. S. McLean, S. K. Ramsay, & H. Takami, 773508
- Bacon, R., Adam, G., Baranne, A., et al. 1988, in *European Southern Observatory Conference and Workshop Proceedings*, Vol. 30, *Very Large Telescopes and their Instrumentation*, Vol. 2, ed. M. H. Ulrich, 1185
- Bacon, R., Vernet, J., Borisova, E., et al. 2014, *The Messenger*, 157, 13
- Barrera-Ballesteros, J. K., Sánchez, S. F., Espinosa-Ponce, C., et al. 2023, *Rev. Mexicana Astron. Astrofis.*, 59, 213
- Benitez, N., Dupke, R., Moles, M., et al. 2014, arXiv e-prints, arXiv:1403.5237
- Benítez, N., Gaztañaga, E., Miquel, R., et al. 2009, *ApJ*, 691, 241
- Bertin, E. 2011, in *Astronomical Society of the Pacific Conference Series*, Vol. 442, *Astronomical Data Analysis Software and Systems XX*, ed. I. N. Evans, A. Accomazzi, D. J. Mink, & A. H. Rots, 435
- Bertin, E. & Arnouts, S. 1996, *A&AS*, 117, 393
- Blanton, M. R., Bershad, M. A., Abolfathi, B., et al. 2017, *AJ*, 154, 28
- Bundy, K., Bershad, M. A., Law, D. R., et al. 2015, *ApJ*, 798, 7
- Cardelli, J. A., Clayton, G. C., & Mathis, J. S. 1989, *ApJ*, 345, 245
- Cenarro, A. J., Moles, M., Cristóbal-Hornillos, D., et al. 2019, *A&A*, 622, A176
- Cenarro, A. J., Moles, M., Marín-Franch, A., et al. 2014, in *Society of Photo-Optical Instrumentation Engineers (SPIE) Conference Series*, Vol. 9149, *Observatory Operations: Strategies, Processes, and Systems V*, ed. A. B. Peck, C. R. Benn, & R. L. Seaman, 91491I
- Croom, S. M., Lawrence, J. S., Bland-Hawthorn, J., et al. 2012, *MNRAS*, 421, 872
- Dupke, R. A., Benitez, N., Moles, M., et al. 2016, in *American Astronomical Society Meeting Abstracts*, Vol. 227, *American Astronomical Society Meeting Abstracts #227*, 349.17
- Emsellem, E., Schinnerer, E., Santoro, F., et al. 2022, *A&A*, 659, A191
- Infante-Sainz, R., Akhlaghi, M., & Eskandarlou, S. 2024, *Research Notes of the American Astronomical Society*, 8, 22
- Jakobsen, P., Ferruit, P., Alves de Oliveira, C., et al. 2022, *A&A*, 661, A80
- James, P. A., Shane, N. S., Beckman, J. E., et al. 2004, *A&A*, 414, 23
- Kennicutt, Jr., R. C. 1998, *ARA&A*, 36, 189
- Kreckel, K., Emsellem, E., Schinnerer, E., et al. 2021, in *American Astronomical Society Meeting Abstracts*, Vol. 238, *American Astronomical Society Meeting Abstracts*, 310.05
- Le Fèvre, O., Saisse, M., Mancini, D., et al. 2003, in *Society of Photo-Optical Instrumentation Engineers (SPIE) Conference Series*, Vol. 4841, *Instrument Design and Performance for Optical/Infrared Ground-based Telescopes*, ed. M. Iye & A. F. M. Moorwood, 1670–1681
- Lee, J. C., Sandstrom, K. M., Leroy, A. K., et al. 2023, *ApJ*, 944, L17
- Lee, J. C., Whitmore, B. C., Thilker, D. A., et al. 2022, *ApJS*, 258, 10
- Leroy, A. K., Schinnerer, E., Hughes, A., et al. 2021, *ApJS*, 257, 43
- Logroño-García, R., Vilella-Rojo, G., López-Sanjuan, C., et al. 2019, *A&A*, 622, A180
- López-Sanjuan, C., Varela, J., Cristóbal-Hornillos, D., et al. 2019, *A&A*, 631, A119
- López-Sanjuan, C., Vázquez Ramió, H., Xiao, K., et al. 2024, *A&A*, 683, A29
- Lumbreras-Calle, A., López-Sanjuan, C., Sobral, D., et al. 2022, *A&A*, 668, A60
- Miller, B. W., Bureau, M., Verolme, E., et al. 2000, in *Astronomical Society of the Pacific Conference Series*, Vol. 195, *Imaging the Universe in Three Dimensions*, ed. W. van Breugel & J. Bland-Hawthorn, 158
- Moles, M., Benítez, N., Aguerri, J. A. L., et al. 2008, *AJ*, 136, 1325
- Novais, P. M. & Sodr , L. 2019, *MNRAS*, 482, 2717
- Piqueras, L., Conseil, S., Shepherd, M., et al. 2019, in *Astronomical Society of the Pacific Conference Series*, Vol. 521, *Astronomical Data Analysis Software and Systems XXVI*, ed. M. Molinaro, K. Shorridge, & F. Pasian, 545
- Sánchez, S. F., Galbany, L., Walcher, C. J., García-Benito, R., & Barrera-Ballesteros, J. K. 2023, *MNRAS*, 526, 5555
- Sánchez, S. F., Kennicutt, R. C., Gil de Paz, A., et al. 2012, *A&A*, 538, A8
- Schlafly, E. F. & Finkbeiner, D. P. 2011, *ApJ*, 737, 103
- Schlegel, D. J., Finkbeiner, D. P., & Davis, M. 1998, *ApJ*, 500, 525
- Sobral, D., Matthee, J., Best, P. N., et al. 2015, *MNRAS*, 451, 2303
- Sobral, D., Smail, I., Best, P. N., et al. 2013, *MNRAS*, 428, 1128
- Stroe, A. & Sobral, D. 2015, *MNRAS*, 453, 242
- Vázquez-Mata, J. A., Hernández-Toledo, H. M., Avila-Reese, V., et al. 2022, *MNRAS*, 512, 2222
- Vilella-Rojo, G., Logroño-García, R., López-Sanjuan, C., et al. 2021, *A&A*, 650, A68
- Vilella-Rojo, G., Viironen, K., López-Sanjuan, C., et al. 2015, *A&A*, 580, A47

Appendix A: CATALOG

Galaxy	IFU	RA [degrees]	Dec [degrees]	Redshift	Morph.type	H α line
NGC 1087	MUSE	41.6048	-0.49864	0.0056	Sc	H α + [NII]
NGC 628	MUSE	24.1739	15.78366	0.00219	SA_B	H α + [NII]
IC0195	CALIFA	30.93579	14.70932	0.01218	E/SO	-
IC0208	CALIFA	32.11562	6.39509	0.01202	Sa-Sc	H α + [NII]
IC1256	CALIFA	260.94699	26.4865	0.0159	Sb	H α
IC1683	CALIFA	20.6622	34.4371	0.0162	SABb	H α
IC2604	CALIFA	162.35448	32.77264	0.00567	SA	H α + [NII]
NGC0169	CALIFA	9.215	23.991	0.0154	SAab(x)	-, DL
NGC0214	CALIFA	10.3668	25.4994	0.0151	Sbc	H α
NGC0495	CALIFA	20.73271	33.47181	0.0136	S0a	-
NGC0499	CALIFA	20.7979	33.4602	0.0146	E5	-
NGC0504	CALIFA	20.8663	33.2044	0.0141	S0	-
NGC0507	CALIFA	20.91592	33.2564	0.01643	E/S0	-
NGC0517	CALIFA	21.1825	33.4296	0.014	S0	-
NGC0523	CALIFA	21.3365	34.025	0.0162	SdAB(Y)	H α
NGC0528	CALIFA	21.3899	33.6714	0.0161	S0	-
NGC0529	CALIFA	21.4178	34.713	0.0163	E4	-
NGC0693	CALIFA	27.6302	6.1445	0.0052	Sa	H α + [NII]
NGC0825	CALIFA	32.1347	6.3237	0.0115	SAa	-, DL
NGC0962	CALIFA	38.1659	28.07	0.0155	E	-
NGC1026	CALIFA	39.83	6.544	0.014	S0	-
NGC1070	CALIFA	40.8428	4.9683	0.0137	SbA(N)	H α + [NII]
NGC2410	CALIFA	113.7594	32.8221	0.0156	Sb	H α
NGC2476	CALIFA	119.1883	39.9279	0.0124	E6	-
NGC2543	CALIFA	123.2414	36.2546	0.0082	SA_B	H α + [NII]
NGC2638	CALIFA	130.60741	37.221	0.0129	S_AB	N, DL
NGC2691	CALIFA	133.69295	39.53878	0.01348	SA	H α + [NII], DL
NGC2780	CALIFA	138.18478	34.92559	0.00649	SBab	H α + [NII]
NGC2916	CALIFA	143.74001	21.7053	0.0124	Sbc	H α + [NII]
NGC3395	CALIFA	162.45821	32.9801	0.0052	SA	H α + [NII], inter
NGC3600	CALIFA	168.96669	41.59108	0.0022	SA	H α + [NII]
NGC3687	CALIFA	172.0025	29.5111	0.0083	SBbc	H α + [NII]
NGC4185	CALIFA	183.3425	28.511	0.0129	Sbc	H α + [NII]
NGC4210	CALIFA	183.81599	65.9853	0.0091	Sb	H α + [NII]
NGC4644	CALIFA	190.6778	55.1455	0.0164	Sb	H α
NGC5198	CALIFA	202.54739	46.6707	0.0085	E/S0	-
NGC5443	CALIFA	210.54919	55.814	0.006	SAB_x	-
NGC5473	CALIFA	211.1801	54.8926	0.0066	E/SO	-
NGC5475	CALIFA	211.3017	55.7419	0.0058	SA	-
NGC5485	CALIFA	211.7973	55.0016	0.0064	E5	-, DL
NGC5631	CALIFA	216.6387	56.5826	0.0066	SA: E/SO	N, DL
NGC5635	CALIFA	217.13229	27.409	0.0144	SaA(N)	N, ?
NGC5659	CALIFA	217.7756	25.3551	0.015	SA	H α
NGC5687	CALIFA	218.71831	54.4759	0.0072	E/S0	-
NGC5714	CALIFA	219.548	46.6382	0.0075	SA	H α + [NII]
NGC5730	CALIFA	219.9673	42.7423	0.0084	S	H α + [NII]
NGC5731	CALIFA	220.03841	42.7795	0.0084	SAc	H α + [NII]
NGC5876	CALIFA	227.3815	54.5065	0.0109	S0a	-
NGC5908	CALIFA	229.17999	55.4096	0.0112	Sa	H α + [NII]
NGC5971	CALIFA	233.9037	56.4617	0.0113	Sb	H α + [NII], low
NGC6278	CALIFA	255.2097	23.011	0.0093	S0a	-
NGC6411	CALIFA	263.8869	60.8134	0.0123	E4A	-
NGC7549	CALIFA	348.82199	19.0418	0.0157	Sbc	H α
MCG+09-22-53	CALIFA	200.63538	54.81829	0.01183	Scd	H α + [NII]
SDSSJ100141.02+371447.4	CALIFA	150.42149	37.2477	0.0052	Irr	H α + [NII]
UGC00139	CALIFA	3.6328	-0.7376	0.0132	SA	H α + [NII]
UGC00987	CALIFA	21.381	32.1363	0.0155	Sa	H α , DL
UGC02134	CALIFA	39.7159	27.8473	0.01539	SbA(N)	H α
UGC03899	CALIFA	113.1573	35.6145	0.0129	SA	H α + [NII]
UGC03944	CALIFA	114.6521	37.6335	0.013	SA	H α + [NII]
UGC03960	CALIFA	115.09474	23.27495	0.00755	E	-
UGC04029	CALIFA	117.079	34.3323	0.0148	Sc	H α
UGC04176	CALIFA	120.6785	40.6786	0.0105	SdAB(N)	H α + [NII]
UGC05326	CALIFA	148.85193	33.26281	0.00477	SA	H α + [NII]
UGC06517	CALIFA	173.01007	36.69794	0.00838	S_AB	H α + [NII]
UGC07129	CALIFA	182.22952	41.74084	0.00308	SB	H α + [NII]

Table A.1 continued from previous page

Galaxy	IFU	RA [degrees]	Dec [degrees]	Redshift	Morph.type	H α line
UGC08733	CALIFA	207.16251	43.4125	0.0078	Sdm	H α + [NII]
UGC08984	CALIFA	210.9465	35.7417	0.0127	S	–
UGC09056	CALIFA	212.33815	49.03957	0.0067	Sd	H α + [NII]
UGC09071	CALIFA	212.51289	54.2183	0.0063	SAB	H α + [NII]
UGC09476	CALIFA	220.3835	44.5128	0.0109	Sbc	H α + [NII]
UGC9562	CALIFA	222.81007	35.54239	0.00416	Im/BCD	H α + [NII]
UGC9663	CALIFA	225.30692	52.59641	0.008	S/IA	H α + [NII]
UGC09665	CALIFA	225.3853	48.3197	0.0085	Sb	H α + [NII]
UGC09759	CALIFA	227.6713	55.3493	0.0115	SabA(N)	N, DL
UGC09849	CALIFA	231.3185	53.4071	0.0116	SB	H α + [NII]
UGC09937	CALIFA	234.3455	20.5498	0.0149	S	–
UGC10043	CALIFA	237.1725	21.8698	0.0072	S	–, DL
UGC10123	CALIFA	239.7623	51.3047	0.0126	Sab	H α + [NII]
UGC10650	CALIFA	255.06081	23.1063	0.0099	Scd	H α + [NII]
MaNGA-8135-6101	MaNGA	115.24227	39.3793235	0.01085	IrrAB	H α + [NII]
MaNGA-8139-3702	MaNGA	114.758707	33.9160464	0.013052	SABdm	H α + [NII]
MaNGA-8139-6103	MaNGA	114.190162	33.1227527	0.016195	SBd	H α
MaNGA-8139-12701	MaNGA	115.479933	31.4115351	0.015588	Sbc	H α
MaNGA-8139-12703	MaNGA	114.04749	32.5151467	0.013843	Sm	H α + [NII]
MaNGA-8139-12704	MaNGA	115.042929	32.2064393	0.013539	Sc	H α + [NII]
MaNGA-8145-3701	MaNGA	117.104738	27.5752478	0.01558	Sbc	H α
MaNGA-8145-3702	MaNGA	116.379534	28.4410097	0.015765	Sb	H α
MaNGA-8145-3703	MaNGA	117.325283	28.4734871	0.01609	Sa	–
MaNGA-8145-6102	MaNGA	116.553531	26.9230031	0.015731	S0	–
MaNGA-8145-9102	MaNGA	116.660474	26.4702171	0.015368	SBbc	H α
MaNGA-8145-12705	MaNGA	117.009656	28.4049994	0.015773	Sd	H α
MaNGA-8147-1902	MaNGA	117.177505	26.5397644	0.015496	Sa	H α
MaNGA-8147-3702	MaNGA	116.59948	27.3382112	0.016007	Scd	H α
MaNGA-8147-6101	MaNGA	116.620888	26.7181168	0.015263	SABc	H α
MaNGA-8147-9102	MaNGA	118.852821	26.9863498	0.015236	SABcd	H α
MaNGA-8148-12704	MaNGA	119.249122	27.754889	0.016499	Sc	H α
MaNGA-8150-3702	MaNGA	147.867177	32.943657	0.004653	SBd	H α + [NII]
MaNGA-8150-6103	MaNGA	147.14825	33.4216194	0.00493	Sd	H α + [NII]
MaNGA-8152-12702	MaNGA	141.427676	34.8564484	0.016264	Sd	H α
MaNGA-8152-12703	MaNGA	141.4273	35.3060457	0.016338	Sbc	H α
MaNGA-8152-12704	MaNGA	142.410329	35.3402379	0.014521	SABm	H α + part[NII]
MaNGA-8309-3703	MaNGA	210.623588	54.2710048	0.000507	M101, SF region	H α + [NII]
MaNGA-8462-12702	MaNGA	145.202128	36.4555403	0.014714	SBd	H α
MaNGA-8546-12702	MaNGA	236.298151	51.1015699	0.012476	Scd	H α + [NII]
MaNGA-8553-3701	MaNGA	233.49151	56.8473196	0.010808	Ede	–
MaNGA-8553-6101	MaNGA	233.352287	56.6087572	0.011784	Sb	–
MaNGA-8553-12702	MaNGA	233.509524	56.6856855	0.012038	SBbc	–, DL
MaNGA-8553-12703	MaNGA	235.953175	57.2332325	0.013553	SBd	H α + [NII]
MaNGA-8554-12704	MaNGA	183.03892	36.16891	0.000544	dSph	H α + [NII]
MaNGA-8562-12702	MaNGA	242.80915	51.1923715	0.012983	Sc	H α + [NII]
MaNGA-8565-6104	MaNGA	242.797968	48.3344561	0.009435	SBdm	H α + [NII]
MaNGA-8566-6103	MaNGA	113.898296	41.9635889	0.010338	Sbc	H α + [NII]
MaNGA-8567-12701	MaNGA	119.25776	49.5673729	0.011684	Sc	H α + [NII]
MaNGA-8589-3704	MaNGA	228.754043	55.4320093	0.010554	S0	H α + [NII]
MaNGA-8591-3703	MaNGA	212.468001	54.447036	0.016449	Sa	H α
MaNGA-8596-6103	MaNGA	230.20908	49.51394	0.015154	Sdm	H α
MaNGA-8612-12703	MaNGA	254.014682	39.6455015	0.015658	Sc	H α
MaNGA-8710-12703	MaNGA	119.24546	50.634535	0.016285	Sm	H α
MaNGA-8713-3701	MaNGA	117.061131	39.0457307	0.013528	SABc	H α + [NII]
MaNGA-8717-12705	MaNGA	119.366691	35.7204534	0.013886	Sd	H α + [NII]
MaNGA-8720-12704	MaNGA	122.354797	50.2638982	0.016377	Sc	H α
MaNGA-8934-3701	MaNGA	194.02549	27.67798	0.016483	Sm	H α
MaNGA-8936-3703	MaNGA	117.54378	30.68509	0.01479	SBd	H α + part[NII]
MaNGA-8936-6104	MaNGA	117.929432	30.4487516	0.01424	SBm	H α + [NII]
MaNGA-8936-12703	MaNGA	118.053469	30.3577362	0.014365	SBd	H α + part[NII]
MaNGA-8936-12704	MaNGA	116.825263	30.9904275	0.012683	SABcd	(H α + [NII])
MaNGA-8938-12705	MaNGA	121.06602	30.18235	0.013836	Sc	H α + [NII]
MaNGA-8977-12704	MaNGA	116.980812	34.0367067	0.015871	Sm	H α
MaNGA-8981-12705	MaNGA	187.902643	36.0074993	0.005748	Sbc	H α + [NII]
MaNGA-8986-3702	MaNGA	119.607231	28.7037153	0.014016	SABb	H α + part[NII]
MaNGA-9034-12701	MaNGA	225.059027	46.436239	0.015503	SABc	H α
MaNGA-9183-6102	MaNGA	122.135233	38.9053417	0.012434	S0	–
MaNGA-9184-1902	MaNGA	119.267946	33.0890111	0.016311	Sab	–

Table A.1 continued from previous page

Galaxy	IFU	RA [degrees]	Dec [degrees]	Redshift	Morph.type	H α line
MaNGA-9195-12703	MaNGA	30.183128	14.2106206	0.015972	SBbc	H α
MaNGA-9484-1902	MaNGA	120.439771	34.7578795	0.015537	SABbc	H α
MaNGA-9484-12701	MaNGA	118.607587	35.0728724	0.014155	Sbc	H α + part[NII]
MaNGA-9486-3701	MaNGA	122.002817	39.1629728	0.01275	Ede?	H α + [NII]
MaNGA-9486-3704	MaNGA	122.052017	39.6603945	0.012921	S0	–
MaNGA-9493-3702	MaNGA	128.693825	23.7174532	0.016492	Sc	H α
MaNGA-9493-12702	MaNGA	129.012734	23.9118396	0.01218	SABd	H α + [NII]
MaNGA-9863-12704	MaNGA	195.068828	27.9675169	0.01547	Sb	–
MaNGA-9865-1901	MaNGA	222.436849	50.7108933	0.01342	SAB0	H α + [NII]
MaNGA-9865-6101	MaNGA	225.102418	49.254069	0.014384	Sc	H α + part[NII]
MaNGA-9866-6103	MaNGA	243.58797	32.1765753	0.014507	Sb	H α + [NII]
MaNGA-9875-6104	MaNGA	194.917112	27.8549331	0.012672	S0	–
MaNGA 9877-6104	MaNGA	195.090291	27.8985596	0.016259	S0a	–
MaNGA-9889-6102	MaNGA	234.78984	24.8308932	0.016204	Sm	H α
MaNGA-10001-12704	MaNGA	133.989967	57.6779677	0.014122	Sd	H α + part [NII]
MaNGA 10500-12703	MaNGA	137.160233	32.5929527	0.014229	Sb	H α
MaNGA-10508-12704	MaNGA	183.883908	51.9130382	0.013393	Sd	H α + [NII]
MaNGA 11013-6102	MaNGA	206.810497	55.5696185	0.015547	SBm	H α
MaNGA-11020-12701	MaNGA	202.68707	54.91083	0.000207	dSph	H α + [NII]
MaNGA-11939-3703	MaNGA	194.355202	27.4045722	0.016175	SABa	H α
MaNGA-11953-12705	MaNGA	190.842661	42.4792377	0.014115	Sdm	H α + part [NII]
MaNGA-12483-9102	MaNGA	186.453995	33.5469017	0.001064	SABd	H α + [NII]
MaNGA-12622-6102	MaNGA	201.139465	31.671516	0.015664	S0a	–
MaNGA-12622-12704	MaNGA	201.02653	31.76235	0.015435	SABc	H α

Table A.1: Cross match catalog of J-PLUS with CALIFA, MaNGA and MUSE. Column 1-7: Galaxy name, IFU, RA and DEC, redshift, Morphological type, and presence of H α line in their IFU spectra. The morphology of the MaNGA sample is taken from [Vázquez-Mata et al. \(2022\)](#) and the morphology type of CALIFA galaxies are from NED database.

Appendix B: Additional figures

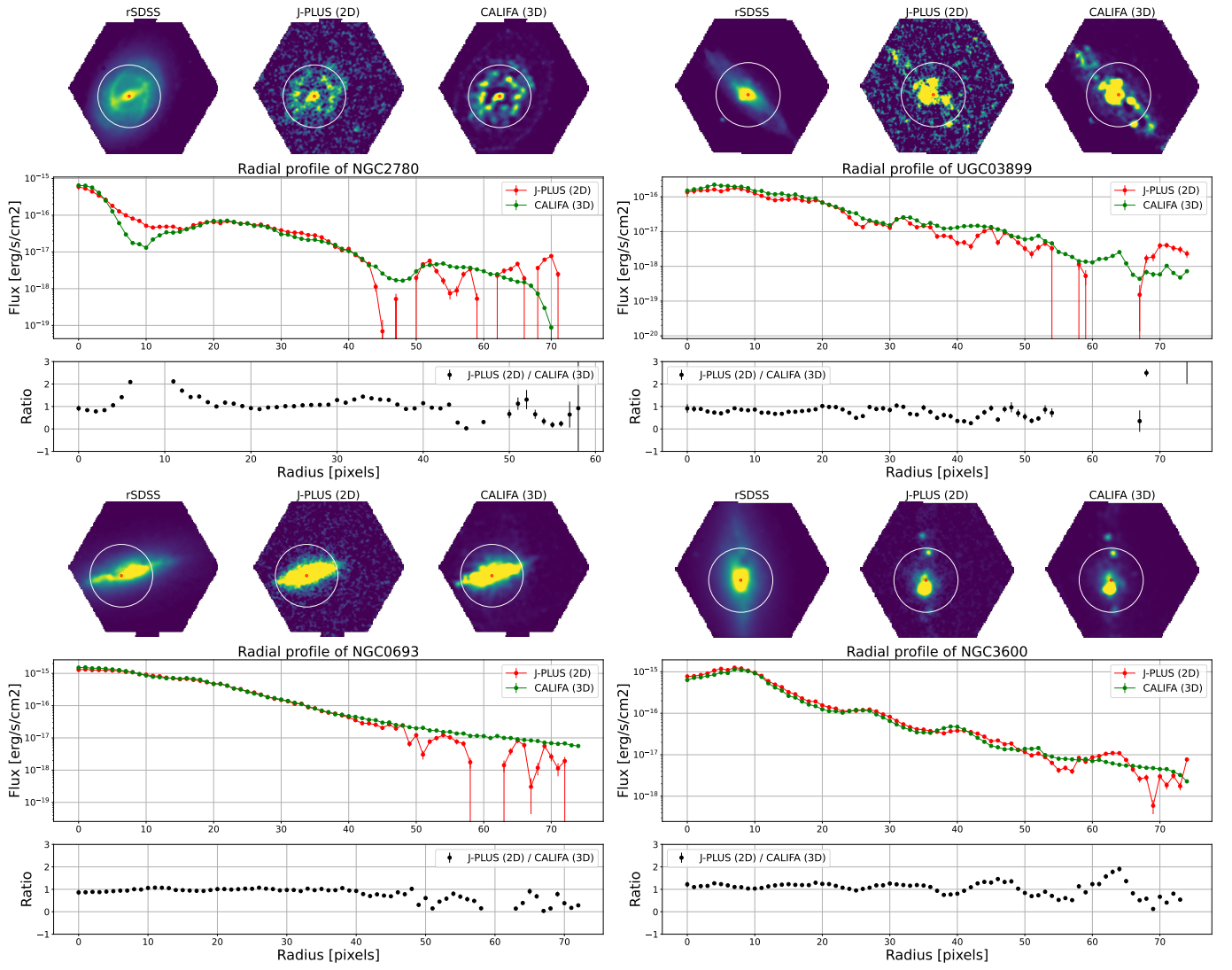


Fig. B.1: Upper: rSDSS, J-PLUS (2D), and CALIFA (3D) H α map images of galaxies. Middle: Radial profiles of J-PLUS (2D), and CALIFA (3D) H α maps. Lower: The ratio of the radial profiles J-PLUS (2D)/CALIFA (3D)

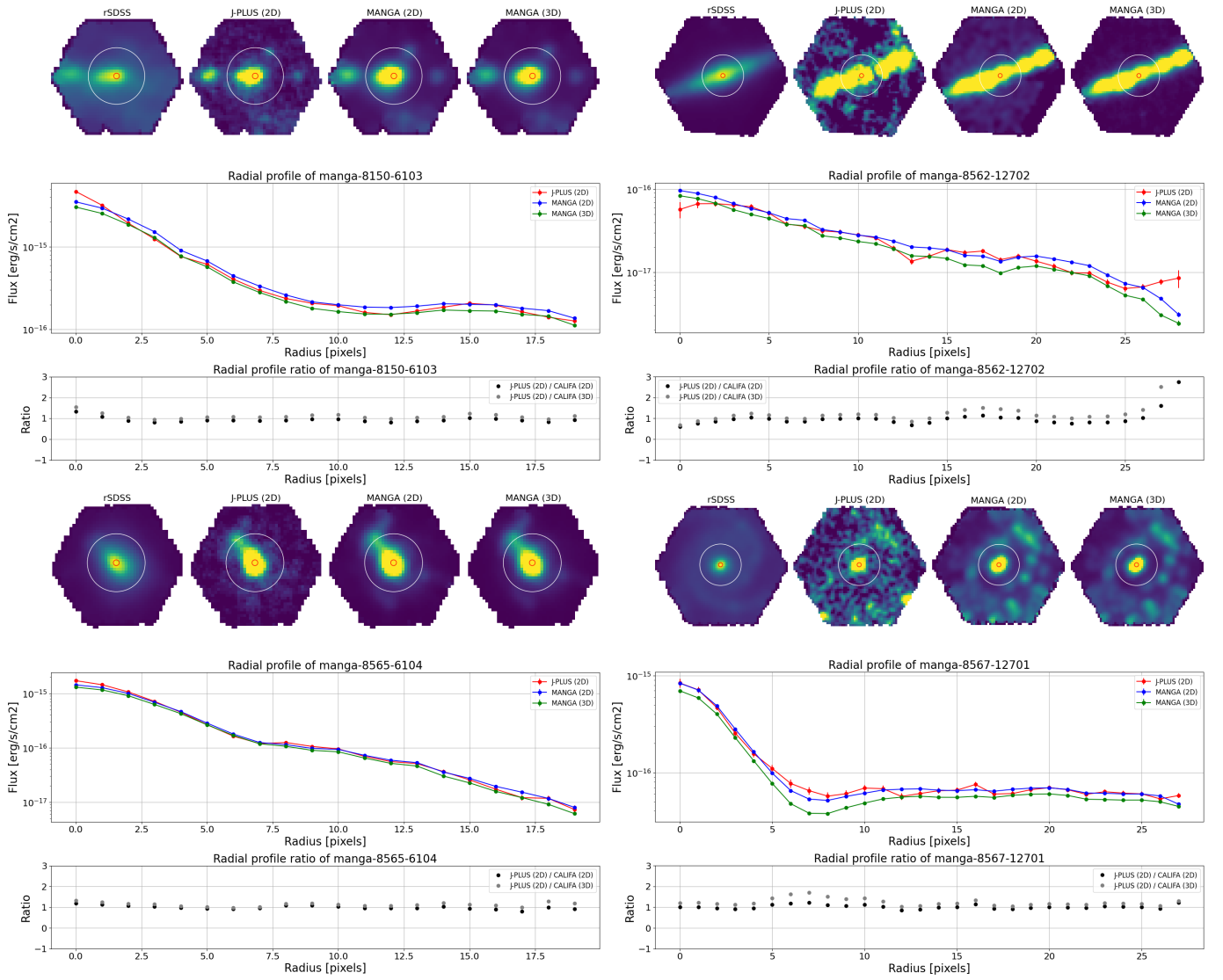


Fig. B.2: Upper: rSDSS, J-PLUS (2D), MaNGA (2D) and MaNGA (3D) H α map images of galaxies. Middle: Radial profiles of J-PLUS (2D), MaNGA (2D) and MaNGA (3D) H α maps. Lower: The ratio of the radial profiles J-PLUS (2D)/MaNGA (2D)